JGR Solid Earth

RESEARCH ARTICLE
10.1029/2020JB021496

Special Section:
Ophiolites and Oceanic Lithosphere, with a focus on the Samail ophiolite in Oman

Quantifying the Axial Magma Lens Dynamics at the Roof of Oceanic Magma Reservoirs (Dike/Gabbro Transition): Oman Drilling Project GT3 Site Survey

Lydéric France[1], Maéva Lombard[1], Christian Nicollet[2], Carole Berthod[1,2], Baptiste Debret[3], Juergen Koepke[4], Benoit Ildefonse[5], and Aurore Toussaint[1,6]

[1]Université de Lorraine, CNRS, CRPG, Nancy, France, [2]Laboratoire Magmas et Volcans, Université Clermont Auvergne - CNRS - IRD, OPGC, Aubière, France, [3]Université de Paris, Institut de Physique du Globe de Paris, CNRS, Paris, France, [4]Institut fuer Mineralogie, Universitaet Hannover, Hannover, Germany, [5]Géosciences Montpellier, Université de Montpellier, CNRS, Montpellier, France, [6]Institute of Earth Sciences, University of Lausanne, Lausanne, Switzerland

Key Points:

- At fast-spreading ridges magma-hydrothermal interactions are extensive at roof of axial magma lenses (AML) that are fed by primitive MORB
- AML are transient igneous bodies that provide heat to hydrothermal vents on the seafloor through conductive boundary layers
- AML crystallize to form the isotropic gabbros in decades, and released heat modifies the intruded dike and gabbro hosts

Supporting Information:

Supporting Information may be found in the online version of this article.

Correspondence to:

L. France,
lyderic.france@univ-lorraine.fr

Citation:

France, L., Lombard, M., Nicollet, C., Berthod, C., Debret, B., Koepke, J., et al. (2021). Quantifying the axial magma lens dynamics at the roof of oceanic magma reservoirs (dike/gabbro transition): Oman drilling project GT3 site survey. *Journal of Geophysical Research: Solid Earth*, *126*, e2020JB021496. https://doi.org/10.1029/2020JB021496

Received 8 DEC 2020
Accepted 19 MAR 2021

Abstract At oceanic spreading centers, the interactions between the igneous system that builds the crust, and the hydrothermal system that cools it govern the plumbing system architecture and its thermokinetic evolution. At fast-spreading centers, most of those interactions occur around the axial magma lens (AML) that feeds the upper crust, and possibly part of the underlying mushy igneous reservoir. Heat extracted from crystallizing AML is transferred through a conductive boundary layer to the overlying hydrothermal system. Quantifying the AML physical and thermal evolutions and its interactions with hydrothermal system is therefore essential to understand oceanic accretion. Those general issues were the rationale of drilling ICDP OmanDP Hole GT3A, and we present herein the geological, structural, and petrological data that were used as a site survey to select its location. GT3 area enables observations in three dimensions of fossilized AMLs and overlying dikes. The new field data and corresponding mineral compositions are used together with thermokinetic and thermodynamic models to deliver an integrated dynamic model for the AML/hydrothermal system interactions. Results attest that the isotropic gabbro interval is composite, with gabbro bodies intruding and reheating both gabbros and dikes (up to 1,040°C). We show that AMLs should be considered as transient igneous bodies that likely crystallize from primitive MORBs in decades, releasing heat to the intruded hosts, and feeding high temperature vents on the seafloor. We show for the first time that the thermal gradient recorded in AML roof is consistent with the heat fluxes reported at active hydrothermal vents.

1. Introduction

At oceanic fast-spreading centers, the axial magma lens (AML) that top the mushy igneous reservoir is one of the key horizon as it feeds the upper crust and possibly part of the lower crust (e.g., Boudier et al., 1996; Koepke et al., 2011; MacLeod & Yaouancq, 2000; Nicolas et al., 2009, Figure 1); its roof represents the main interface between the magmatic and hydrothermal systems roughly corresponding to the Layer 2/Layer 3 transition (France et al., 2009; Wilson et al., 2006). The cooling and crystallization of this AML likely provides heat to the active hydrothermal vents on the seafloor (e.g., Lowell et al., 2013), and thus is essential for the formation of volcanogenic massif sulphide deposits (e.g., Humphris & Cann, 2000). Geophysical constraints on this transition at fast- and intermediate-spreading ridges highlight (1) that the AML is discontinuous along axis with mush-rich areas (~15–20 km long) alternating with melt-rich zones (~2–4 km long; Carbotte et al., 2013; Singh et al., 1998), or at an even smaller scale (Marjanovic et al., 2015), (2) is 8–120 m thick (Collier & Singh, 1997; Kent et al., 1993; Singh et al., 1999; Xu, Pablo Canales, et al., 2014), and 600–1,700 m wide (Canales et al., 2005; Kent et al., 1990; a maximum width of 4.15 km having been identified by; Kent et al., 1993), and (3) that its depth is varying along axis over hundreds of meters with the melt supply and the axial depth (Carbotte et al., 2006, 2013; Hooft et al., 1997; Lagabrielle & Cormier, 1999; Macdonald et al., 1991). Variations in the AML depth and properties (e.g., crystallinity) have also been interpreted to be directly related to eruptive events, casting for its partial drainage upon eruption (Marjanovic et al., 2014). Several field, structural, and petrological data have led to the elaboration of a dynamic magma lens model where the AML is a dynamic horizon that can move up or down with the potential to intrude and reheat the root-zone of the sheeted dike complex (SDC; e.g., Coogan et al., 2003; France

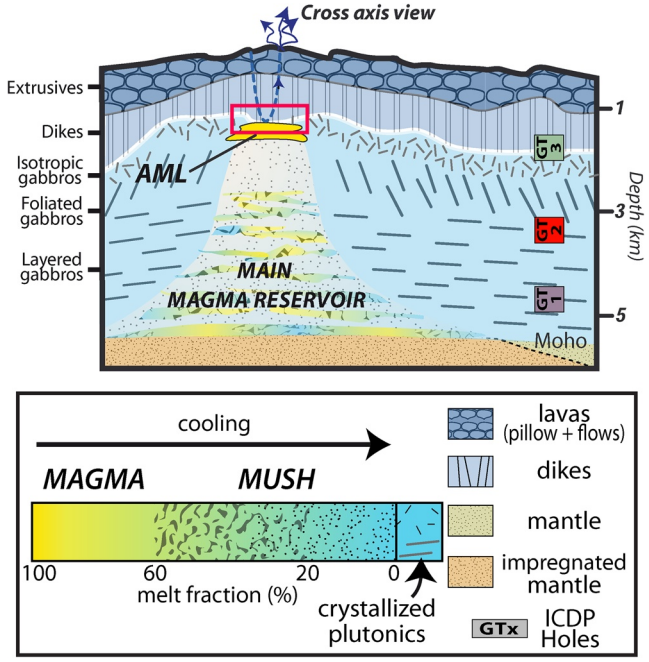

Figure 1. Cross-axis schematic view of the magmatic system and crustal architecture at fast spreading ridges (modified after France et al., 2009). At the ridge axis the likely distribution of melt is documented with melt-rich areas ("magma") possibly forming sills from the Moho level, through the main magma reservoir (that is mostly mushy), to the axial magma lens (AML). Also documented are the crustal section sampled by ICDP OmanDP Holes GT1A, GT2A, and GT3A (Kelemen et al., 2020). Dashed blue curves identify hydrothermal circulations, and the red box documents the section of interest in the present study: the AML roof zone where magma/hydrothermal interactions are intense.

et al., 2009, 2014; Gillis, 2008). The AML may fossilize to form isotropic gabbro with a marked heterogeneity in grain size, texture and composition ("varitextured gabbro"; Coogan et al., 2002; France et al., 2009; Koepke et al., 2011; MacLeod & Yaouancq, 2000; T. Müller et al., 2017) that can be used to constrain the related igneous processes (e.g., France et al., 2013, 2009; Hayman et al., 2019; Koepke et al., 2011; T. Müller et al., 2017; Wilson et al., 2006; Zhang, Koepke, et al., 2017). Here, we aim at quantifying the interactions existing between the magmatic and hydrothermal systems that occur at the roof of the AML and that relate to the AML dynamic character. This study is focused at delivering new constraints on the depth variations of the AML, on the dynamics of reheating stages in the AML roof (maximum reached temperature, reheating temperature range, heat fluxes through the conductive boundary layer and relation to active hydrothermal vents, and related durations), and on the fate of the AML itself. Beyond these main objectives, the field data presented herein have been used as a site survey for the ICDP (International Continental Scientific Drilling Program) Oman Drilling Project (OmanDP) Hole GT3A. GT3A main objective was to have a detailed knowledge of the SDC/gabbro transition as this zone is critical to our understanding of the mechanisms of crustal accretion and hydrothermal cooling of the ocean crust (Kelemen et al., 2020).

2. Background

2.1. Oceanic Crust at Fast-Spreading Centers

Ocean crust covers about the two thirds of Earth surface, and half of it formed at fast- and intermediate-spreading centers (e.g., R. D. Müller et al., 2008). There, the formed crustal section is about 6–7 km thick (Aghaei et al., 2014; Barth & Mutter, 1996; Boulahanis et al., 2020; Canales et al., 2003) and characterized from bottom to top by layered, foliated, and isotropic gabbros (the latter being also named varitextured; e.g., MacLeod & Yaouancq, 2000) forming the lower crust, which is topped by the upper crust comprising SDC that fed the overlying pillow lava and lava flow series (Conference Participants, 1972; Gillis et al., 2014; Nicolas et al., 2000, Figure 1). Seismic crustal architecture of fast-to intermediate spreading crustal sections implies 3 layers that are generally interpreted as representing Layer 2A: pillow lavas and lava flows, Layer 2B: the SDC, Layer 3: the plutonic section; the transitions between the layers are nevertheless still not well characterized (e.g., Carlson, 2011; Detrick et al., 1998). This extensive igneous system formed mostly on-axis, where the magmatic reservoir extending from the Moho level to the SDC root is mainly mushy (e.g., Detrick et al., 1987) with less than 18% of interstitial melt (e.g., <5% according to Caress et al., 1992; <10%–15% according to Lamoureux et al., 1999; 2%–18% according to Crawford et al., 1999; and <10% according to Dunn et al., 2000, Figure 1). Only localized melt-rich lenses are present close to the Moho (Canales et al., 2009; Nedimovic et al., 2005, Figure 1), through the lower mushy reservoir (Boddupalli & Canales, 2019; Canales et al., 2009; Carbotte et al., 2020; Marjanovic et al., 2014, 2015, 2018, Figure 1), and at the reservoir roof (Canales et al., 2009; Marjanovic et al., 2015; Sinton & Detrick, 1992, Figure 1) that roughly corresponds to the Layer2/Layer 3 transition. This transition is the locus of intense interactions between the magmatic system that feeds the crust and the hydrothermal system that cools it (e.g., France et al., 2009; Nehlig, 1993; Zhang, Wang, et al., 2017). Heat extraction at oceanic spreading centers is indeed assisted by an extensive hydrothermal convecting system (e.g., Alt et al., 2010) that is likely facilitated by normal faults (Hayman & Karson, 2009), and mainly develops along axis (e.g., Marjanovic et al., 2017; Nehlig et al., 1994; Tolstoy et al., 2008). Although more prominent in the upper crust, some authors speculate that these systems also extends down section to the Moho level (Abily et al., 2011; Bosch et al., 2004; Currin et al., 2018; Nicolas et al., 2003; Zihlmann et al., 2018).

2.2. Previous Field and Petrologic Constraints on the SDC/Gabbro Transition

The SDC/gabbro transition has been extensively described in Troodos and Oman ophiolites that are interpreted as analogs of fast-spreading oceanic centers (e.g., France et al., 2009; Gillis, 2002; Gillis & Coogan, 2002; Gillis & Roberts, 1999; MacLeod & Rothery, 1992; Nicolas et al., 2008; Nicolas & Boudier, 1991; Rothery, 1983). This transition was also sampled *in situ* at the East Pacific Rise in the Cocos Plate at the ODP Hole 1256D (France et al., 2009; Koepke et al., 2008; Koepke and Zhang, 2020; Teagle et al., 2012; Wilson et al., 2006). At all those locations gabbros are intrusive in the SDC root that is reheated by the corresponding intrusive event (e.g., Coogan et al., 2003; France et al., 2009; France, Koepke, et al., 2010a; Koepke et al., 2008). The reheating event has the potential to trigger hydrous anatexis of the SDC root (hydrous solidus < 850°C; France, Ildefonse, et al., 2010; France, Koepke, et al., 2010), and to produce melts similar to the bulk composition of most of the oceanic plagiogranites that are observed close to the SDC root (Erdmann et al., 2015, 2017; France et al., 2014; France, Koepke, et al., 2010; Gillis & Coogan, 2002; Grimes et al., 2013; see Coleman & Peterman, 1975, and Koepke et al., 2007 for a discussion on the use of the term oceanic plagiogranite that includes all oceanic felsic rocks). If not crystallized as oceanic plagiogranites, the corresponding anatectic melts can mix within the AML contaminating MORB melts at crustal levels (Coogan, 2003; Coogan et al., 2003; Erdmann et al., 2017; Fischer et al., 2016; France et al, 2009, 2014; Gillis et al., 2003; Koepke et al., 2011; Michael & Cornell, 1998; Nehlig, 1993; Wanless et al, 2010, 2011). The base of the SDC has been identified to be texturally and chemically different (over tens of meters) of the overlying SDC section; it is recrystallized to hornfels-like granoblastic assemblages as a consequence of a re-heating event due to contact metamorphism likely triggered by magma intrusion(s) in the SDC root (France et al, 2009, 2014; France, Koepke, et al., 2010; Gillis, 2002, 2008; Gillis & Coogan, 2019; Gillis & Roberts, 1999; Koepke et al., 2008). Granoblastic assemblages can be both recrystallized dehydrated rocks, or igneous residue resulting from a hydrous anatexis stage associated with oceanic plagiogranite formation (e.g., Coogan et al., 2003; Gillis & Coogan, 2002; Erdmann et al., 2015, 2017; France et al, 2014; France, Koepke, et al., 2010). Strong constraints based on experimental petrology, and related to the reheating of the SDC root are now available, test protoliths with various alteration and recrystallization grades, and document recrystallization under both metamorphic and anatectic conditions (Erdmann et al, 2015, 2017; Fischer et al., 2016; France et al, 2014; France, Koepke, et al., 2010). Below the SDC/gabbro transition, the upper isotropic gabbros (or varitextured gabbros) represent a highly heterogeneous plutonic interval that is mainly composed of fine-grained isotropic gabbros with subordinated coarse-grained gabbros, microgranular enclaves or domains that are remnants of partially digested granoblastic dikes, felsic (or plagiogranitic) and Fe-Ti gabbroic patches or veins (e.g., France et al., 2009; Koepke et al., 2011; MacLeod & Yaouancq, 2000; T. Müller et al., 2017; Wilson et al., 2006). Varitextured gabbros also contain various textural domains characterized by large clinopyroxene oikocrysts, granular domains, spotty gabbros, or domains with a marked foliation which is parallel to the underlying vertically foliated gabbros (Koepke et al., 2011; MacLeod & Yaouancq, 2000; T. Müller et al., 2017; Nicolas et al, 2008, 2009).

Late dikes crosscutting the SDC/gabbro transition are observed in all the studied areas; those are interpreted as highlighting either the presence of a lower level magma lens (e.g., France et al., 2009), or off axis magmatism (e.g., Wilson et al., 2006).

2.3. Quantitative Data on the SDC/Gabbro Transition Dynamics, and Open Questions

Field, structural, and petrological observations were interpreted in the frame of a dynamic magma lens model where the dynamic AML can move up or down, and potentially intrude and reheat the root-zone of the SDC (e.g., Coogan et al., 2003; France et al., 2009, 2014; Gillis, 2008). Although very high prograde temperatures are recorded in the reheated dikes (1,045°C in Koepke et al., 2008; 1,030°C in France et al., 2009; 1,040°C in Gillis & Coogan, 2019) there is currently no data available on the temperature range of the reheating stage (from which low temperature are those dykes reheated?). This temperature range could be of tens or hundreds of degrees, and is a key parameter if we are to fully understand the interactions between the magmatic and hydrothermal systems. The geothermal gradient within the conductive boundary layer that separates the AML of the overlying hydrothermal system remains largely underconstrained as it has been estimated to be of 3–4°m^{-1} (Gillis & Coogan, 2019; Koepke et al., 2008) when active vents heat fluxes predict gradients of tens to hundreds of degrees (e.g., Lowell et al., 2013). Also AML migrations (upward

and downward) have been interpreted from several field results in both ophiolites and present day oceanic crust; the vertical extent of such magma lens variations nevertheless remains elusive, and has to be quantified. Even the fact that the AML itself experience vertical migrations may be questioned. Indeed, Fontaine et al. (2011) and Zhang et al. (2014) have shown that only tens of years are required for a hydrothermal system to cool a newly injected magma batch at the SDC/gabbro transition, challenging the classical view of a permanent or steady state AML. Those striking results are also consistent with recent seismic data from the East Pacific Rise suggesting that the AML could be partially drained during axial eruptions (Marjanovic et al., 2014). Both results suggest that the AML may not be a long lived system, but rather a reservoir that could be drained, partially cooled and crystallized, and likely reinjected as magmatic activity continues. A corresponding open question would thus be whether such various or successive melt intrusions at the AML horizon could be identified in the field, that is, complex intrusive successions or reheating effects within the varitextured gabbros themselves. In the present contribution, we provide new field and petrologic data that will eventually bring new constraints on those various open questions or under-constrained parameters.

3. Geological Context

The Cretaceous Oman ophiolite (~500 × 50 km) is regarded as the best on-land proxy for fast-spreading oceanic crust. Nevertheless controversial debates are on-going since decades, and questioned the mid-ocean ridge (MOR) versus supra-subduction zone initial setting (e.g., Boudier & Nicolas, 2007; MacLeod et al., 2013; Warren et al., 2005, 2007). It is likely that the proposed subduction setting is related to the early stage of obduction (e.g., Boudier et al., 1988; Koepke et al., 2009), and is responsible for a second stage of magmatism ("V2" or "Lassai" lavas) following the major accretion of normal fast-spread crust ("V1" or "Geotimes" lavas; for details, and nomenclature of the lavas see Godard et al., 2003). The area selected for the present study is not notably affected by the late-stage magmatism ("V2"), thus the observed field record described here can be exclusively related to the primary magmatic processes of a "normal" fast-spreading ridge.

The studied area is located in the Wadi Aswad in the Southern Sumail massif (Figure 2; Nicolas et al., 2008), ~40 km NW of the Wadi Gideah described in France et al. (2009), and where ICDP Holes GT1A and GT2A from the OmanDP were drilled (Kelemen et al., 2020).

4. Methods

Field work was conducted to map the studied area in terms of lithologies, structures, and relations between the various units (Figure 3), and to sample at most of the field stations presented in Figure 3. Sites with specific textural features (e.g., enclaves, grain-size variations), with igneous contacts, or with both dikes and gabbros have been studied with greater attention. Specific high resolution sampling has also been conducted at the sites corresponding to points 1 to 4 in Figure 3. Heavily hydrothermally altered samples that do not preserve igneous or high grade metamorphism mineral assemblages were not considered in the following as we focus on high grade metamorphic conditions, and on igneous processes.

Major element mineral compositions and backscattered electron images (BSE) were obtained using a CAMECA SX100 electron probe equipped with 5 spectrometers, and the "Peak sight" operating system (SCMEM: service commun de microscopie électronique et de microanalyses; Université de Lorraine, France, and Laboratoire Magmas & Volcans, Clermont-Ferrand, France). All analyses were performed with a focused and static (fixed) beam, a beam current set to 12 nA, a 15 kV acceleration potential, and Kα emissions for all elements. Counting times were set to 40 s on peak, and 20 s on background. Instrument calibration was performed on natural standards, and matrix correction was based on Pouchou and Pichoir (1991). Mineral composition data used in the present study are documented in Tables S1–S5.

Mineral compositions obtained herein are used to quantify the equilibrium temperatures of specific lithologies that are key to our understanding of the dynamics of the Layer 2/Layer 3 transition. When considering geothermometry, the most important point is to use thermometers that are valid in the considered pressure–temperature–composition range. Here, we use the two-pyroxene QUILF thermometer of Andersen et al. (1993), the amphibole-plagioclase thermometer of Holland and Blundy (1994), a recalibrated version

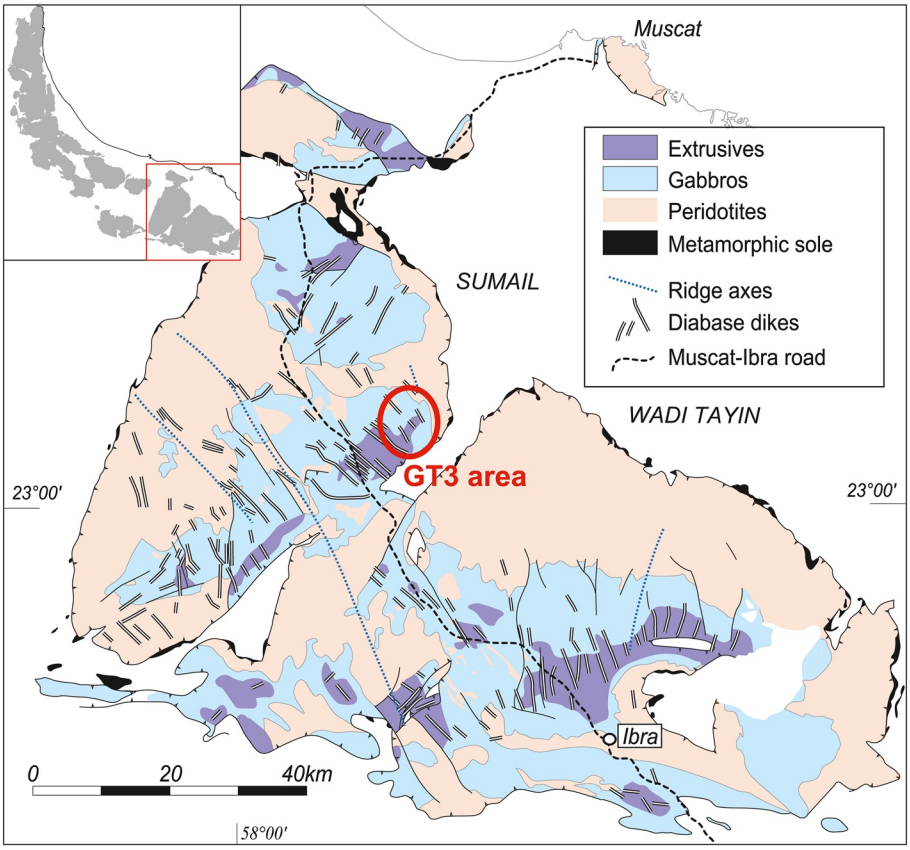

Figure 2. Simplified geological map of the Southern massifs of the Oman ophiolite (from Nicolas et al., 2000). Inset shows the location of the massifs in the Oman ophiolite. The mapped area, corresponding to Wadi Aswad, where the ICDP OmanDP Hole GT3A is located, is localized in the Southern Sumail massif.

of the Ti-in amphibole thermometer of Ernst and Liu (1998), and the Al-in clinopyroxene thermometer of France, Koepke, et al. (2010). The latter was specifically elaborated for the lithologies and conditions of the root zone of the SDC. In the present case, the studied samples are highly heterogeneous because of the intense hydrothermal overprint, which may result in intensely zoned (concentrically or heterogeneously) single grains (mostly amphibole and clinopyroxene). Consequently, the two-mineral thermometers (amphibole-plagioclase and 2-pyroxene) should be used with great caution as those are based on the equilibrium between the two phases. The corresponding temperature estimates will thus be used hereafter as a comparison. However, we will focus our discussion on the results obtained with the Ti-in amphibole and Al-in clinopyroxene thermometers. The Ti-in amphibole thermometer should be used only in systems that contain Fe-Ti oxides. This criterion is respected in the granoblastic assemblages from the SDC root. For gabbros, although most of the studied oceanic gabbros are not *sensu stricto* oxide gabbros, amphibole bearing domains are very commonly oxide-bearing (both amphibole and oxide being commonly present as late interstitial phases), and this thermometer can thus be applied. The recalibration of Ernst and Liu (1998) thermometer has been performed by the Hannover group (Institut für Mineralogie; Leibniz Universität Hannover), and is based on the following equation: $-22.1 \times [TiO_2\,(wt\,\%)]^2 + 220.74 \times [TiO_2\,(wt\,\%)] + 480.7$; it has been tested in experimental studies (France, Koepke, et al., 2010; Koepke et al., 2003), and has been used in several studies (France et al., 2009, 2013; Koepke et al., 2008, 2011). The Al-in clinopyroxene thermometer has been developed experimentally by using an altered dike, considered as representative of the SDC, as a starting material (France, Koepke, et al., 2010). The corresponding experiments were designed to reproduce the reheating processes that are ongoing at the SDC root, and the dike used as starting material was sampled in the Aswad area studied herein; the developed thermometer is therefore particularly well suited for the present study. Erdmann et al. (2015) who conducted similar dike-reheating experiments by

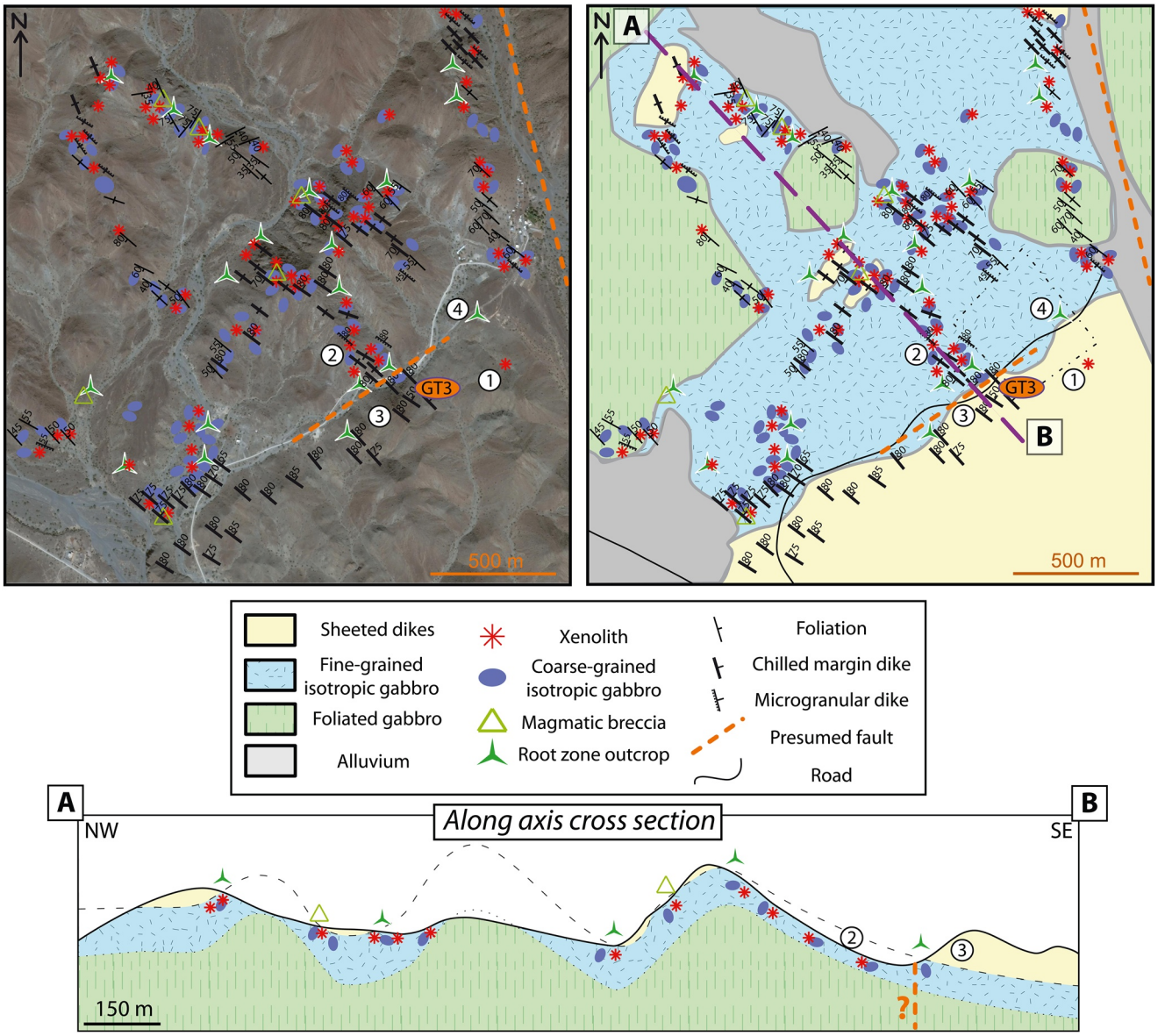

Figure 3. Detailed geological and structural map (top right), and related cross section (line A-B in the map; bottom) of the studied area (no vertical exaggeration). An aerial view derived from Google Earth is also presented along with the field data for easy location of the related outcrops (top left). Points 1 to 4 locate specific outcrops that are discussed in text and in Figures 5–7 and 10. Dashed black line in the cross section displays a theoretical prolongation of the dike/gabbro contact. The kinematics of the presume fault to the SE of the cross section are not known, therefore no offset is documented.

using alternative starting materials from the SDC root sampled at the ODP Hole 1256D, also confirmed the validity of this thermometer.

5. Field Observations

The studied area is ~2.5 × 2.5 km^2 large, and extends from the foliated gabbros to the SDC (Figures 1, 3, and 4a). The SDC in the studied areas is characterized by 0.3–10 m wide dikes (most of the dikes being 1–1.5 m wide) with characteristic chilled margins, and are trending 140°N (Figure 3). Some rare screens of fine-to coarse-grained gabbros are pinched between dikes that chilled against the screens (Figure 3, point 1; Figures 5a–5c). Most of those gabbro screens are observed in the first tens of meters but some rare ones are located at >200 m from the SDC/gabbro contact (Figure 5). Remarkably, the gabbro screen that we have identified within the SDC at the highest distance of the SDC/gabbro transition also contains former

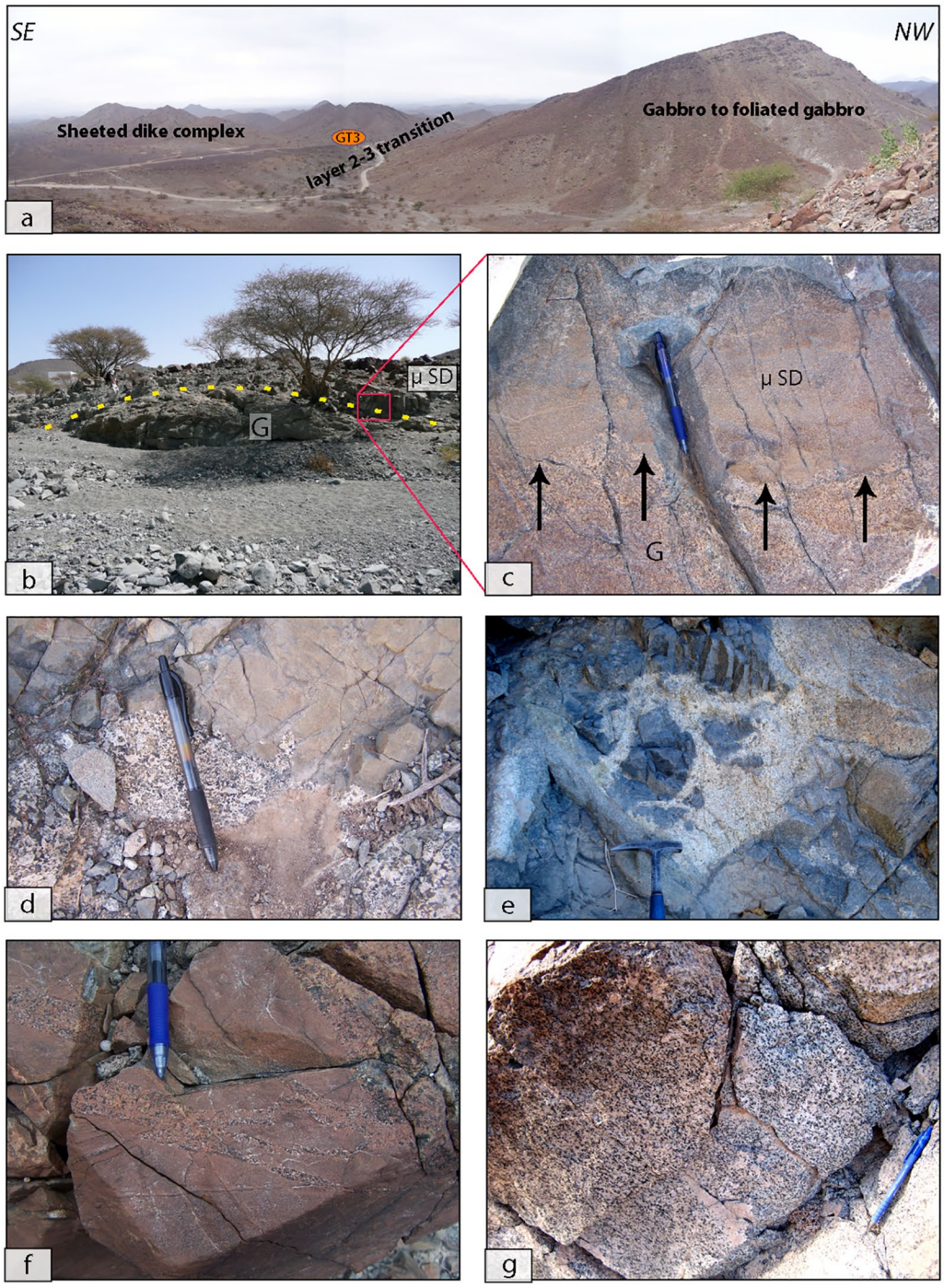

Figure 4. Specific outcrops and field observations of the sheeted dike complex (SDC)/gabbro transition in the Oman ophiolite. (a–f) Dike gabbro transition, and (g–o) various gabbroic facieses. (a) General view of GT3 area in the Wadi Aswad area. ICDP OmanDP Hole GT3A is located in the root zone of the SDC at the transition to gabbros (b and c). Intrusive contact of gabbros (G) in the recrystallized granoblastic dike root zone (μSD) marked in yellow dotted line in (b) Lateral extension of the contact is highlighted in (b) with L. France for scale to the left of the picture; arrows in (c) show the intrusive contact. (d) Other example of gabbros intruding the SDC base. (e) Magmatic breccia composed of gabbros and felsic rocks (the so called oceanic plagiogranites) containing microgranular enclaves of dikes; the outcrop is located directly at the contact between dikes and gabbros. (f) Gabbro injections in the recrystallized microgranular base of the SDC. (g) Archetype of granular foliated gabbros being part of eponymous level in Figures 1 and 3, (h–l) Outcrops documenting the heterogeneity of the gabbroic textures encountered in the isotropic gabbro interval ("varitextured gabbros"). (h) Displays fine grained isotropic gabbro with subordinate coarse-grained domains. Patchy gabbros are characterized by felsic patches (i), granular pyroxenes (j), or subophitic gabbros with large poikilitic clinopyroxenes (k–l) and subordinate leuco-granular domains. "Gabbro in gabbro" intrusive contacts are common in gabbros (m–o); those are sutured and locally overprinted by felsic melt migration (m and n). Arrows in (m) point to the "gabbro in gabbro" intrusive contacts.

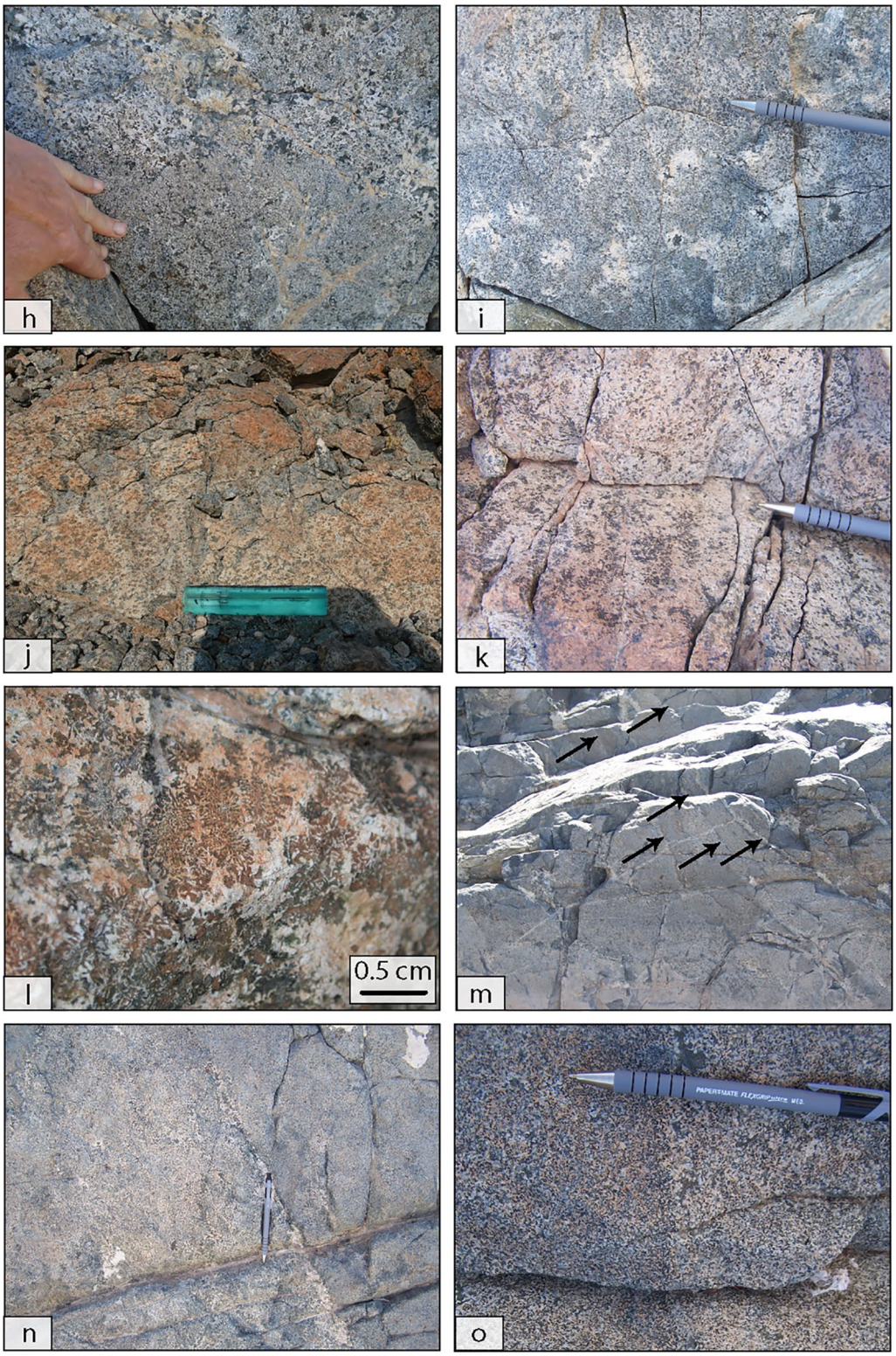

Figure 4. *Continued*

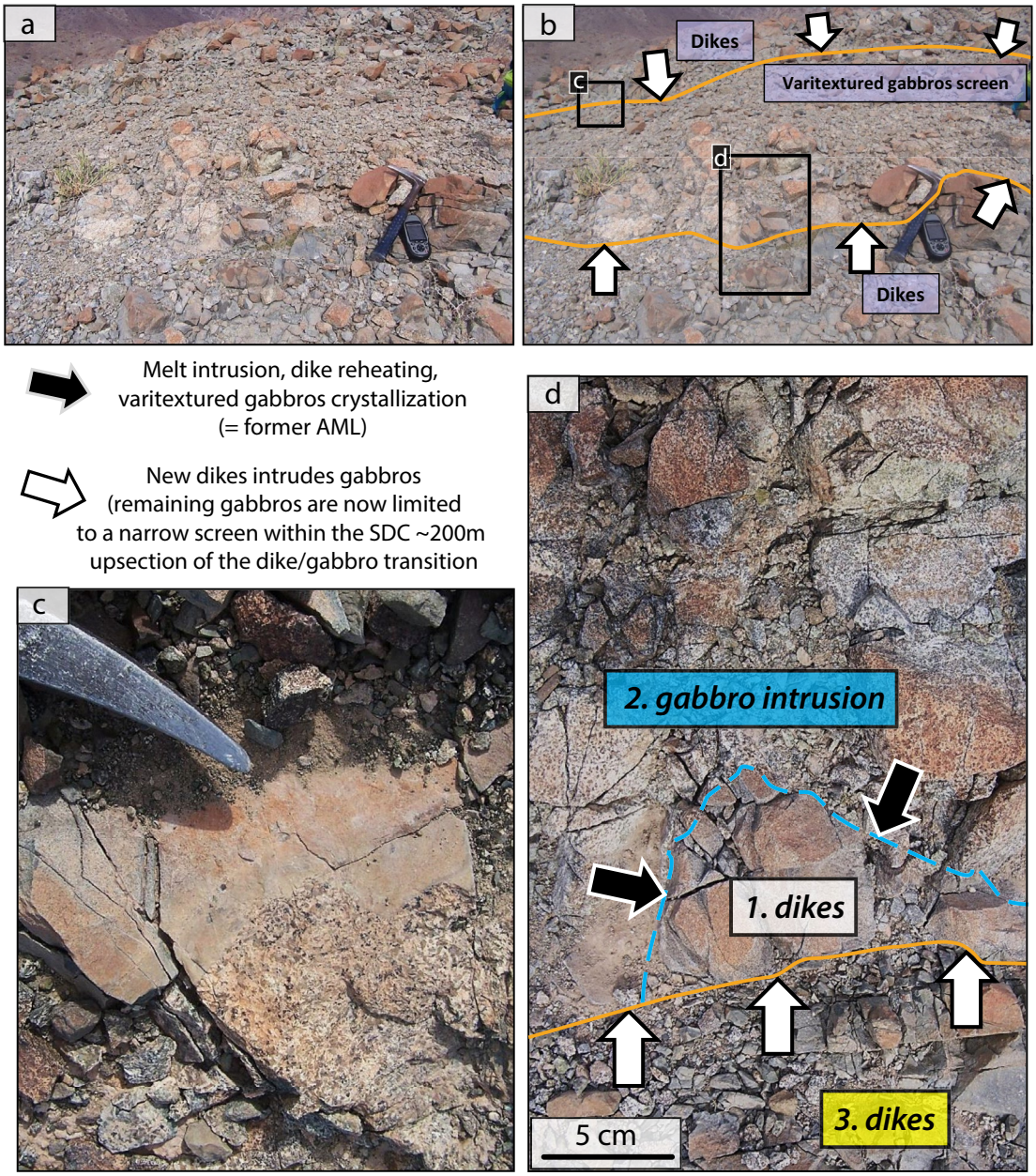

Figure 5. Gabbro screen outcrop (station 1 in Figure 3). (a) is the raw photo of the outcrop that is interpreted in (b) whereas panels (c and d) represent zoomed in areas (indicated in black boxes in panel b). White arrows in (b and d) point to the dikes margins that chilled against the gabbro screen. The chilled margin is also visible in (c). Black arrows in (d) point to the former intrusive contact of the gabbroic body as it contains a microgranular dike piece (interpreted as a formerly stopped dike piece). This outcrop is located within the sheeted dike complex (SDC) ~200 m upsection from the SDC/gabbro transition, and attests to a former high level of the AML.

microgranular enclave (Figure 5d). Down section, close to the SDC/gabbro transition, texture variation in dikes is hard to capture on hand samples (see "key petrological features" section for the presentation of the granoblastic overprint), but microgranular margins are present instead of chilled margins. The contact between the isotropic gabbros and the SDC is observed in several places ("root zone outcrop" in Figure 3; e.g., Figure 6, and is always sharp (Figures 4b–4d, 6a and 6b) and intrusive (Figures 4c, 4d, 4f, 6a, 6b, 7a and 7b). At <10 m of the contact with the SDC the isotropic gabbro contain locally some magmatic breccia composed of several angular to roundish gabbro and microgranular dike enclaves embedded in coarse-to fine-grained plutonic rocks composed of gabbro, diorite, and plagiogranite (e.g., Figures 3 and 4e). Locally root zone outcrops reveal mutual intrusions of several dikes or gabbro bodies (Figure 6). Some rare dikes

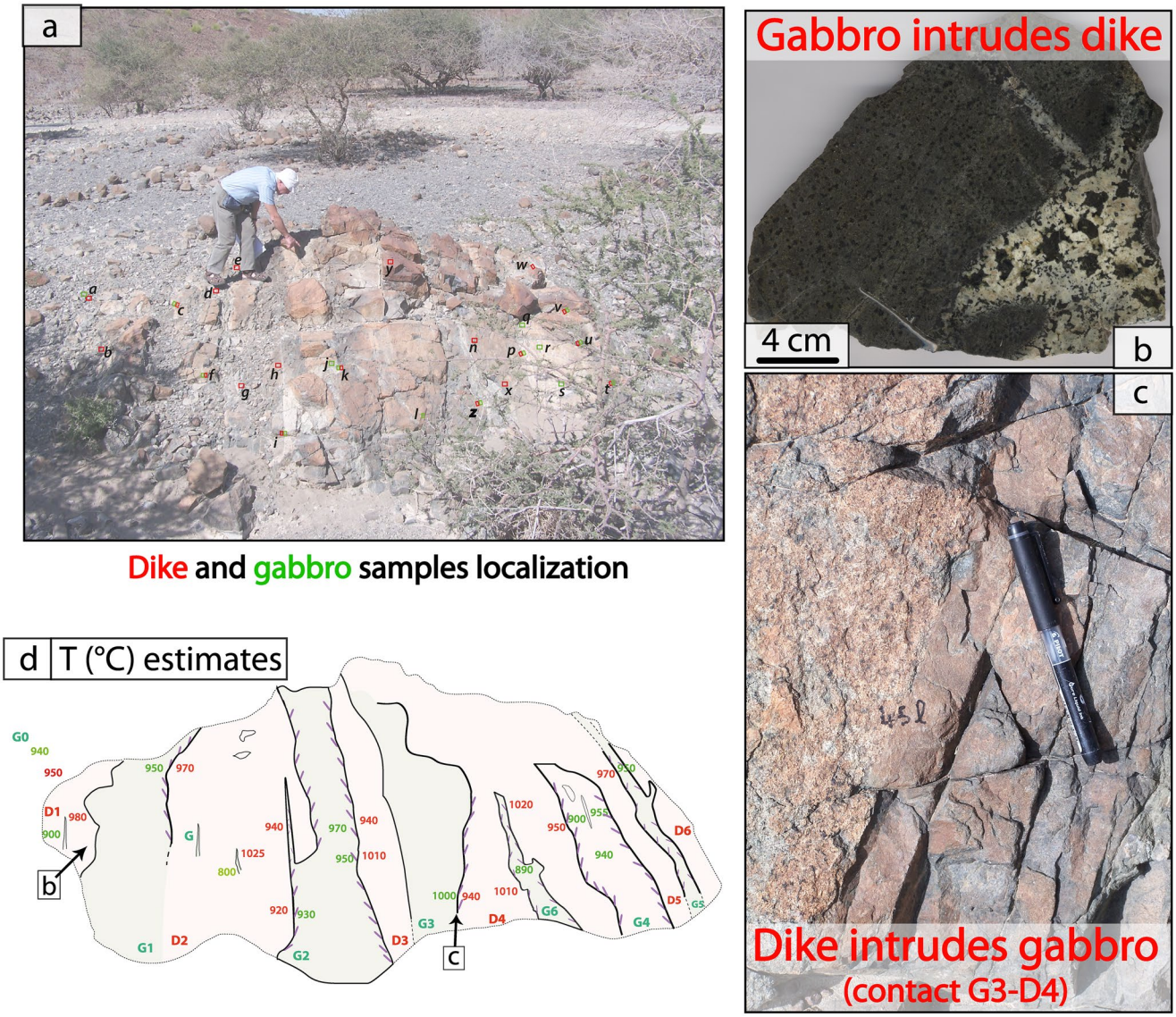

Figure 6. Archetype of a root zone outcrop with mutual intrusion of dikes and gabbros (station 4 in Figure 3). (a) outcrop picture with location of the used samples, small letters represent sample names (from 07OL45a to 07OL45z), red and green boxes represent the sampling locations of dikes and gabbros, respectively; the scale is given by Prof. Adolphe Nicolas. (b) picture of a hand sample (sample 07OL45a) with clear intrusive character of the gabbro in the granoblastic dike. (c) outcrop picture of the contact between G3 and D4 with the dike being intrusive in the gabbro (location of G3 and D4 are documented in d)). The dike is microgranular and might represent an example of a dike root (named protodike in Nicolas & Boudier, 1991; Nicolas et al., 2008; France et al., 2009). (d) Interpretative sketch of the outcrop presented in (a) with various dikes (D1-6), and gabbros (G0-6) identified. The ticks on the intrusions rims are placed on the intruding side. Maximum temperature estimates (in °C) obtained with the Al in clinopyroxene thermometer of France, Koepke, et al. (2010) are also documented for both dikes (red values), and gabbros (green values). "D" and "G" identify individual dikes and gabbros. Corresponding clinopyroxene compositions are presented in Table S1.

with microgranular margins are intrusive in the isotropic gabbros (Figure 6c), and likely represent dikes that root slightly deeper in the section as previously described by France et al. (2009), Nicolas et al. (2008), Nicolas and Boudier (1991) (such microgranular dike roots were named protodikes by those authors). Coarse-grained isotropic gabbros are abundant within the isotropic gabbro interval (Figure 3), and as reported elsewhere in the root zone of the SDC are locally concentrated around the microgranular xenoliths (Figure 3; e.g., France et al., 2009). Microgranular xenoliths are present at nearly all the root zone outcrops (Figures 3 and 4e), but are also observed sparsely in the isotropic gabbro interval. Oceanic plagiogranite domains and patches are common in the isotropic gabbros close to the SDC base (e.g., Figure 4e) or close to gabbro in gabbro intrusive contacts (Figures 4i, 4m, and 4n). The isotropic gabbro interval (or varitextured

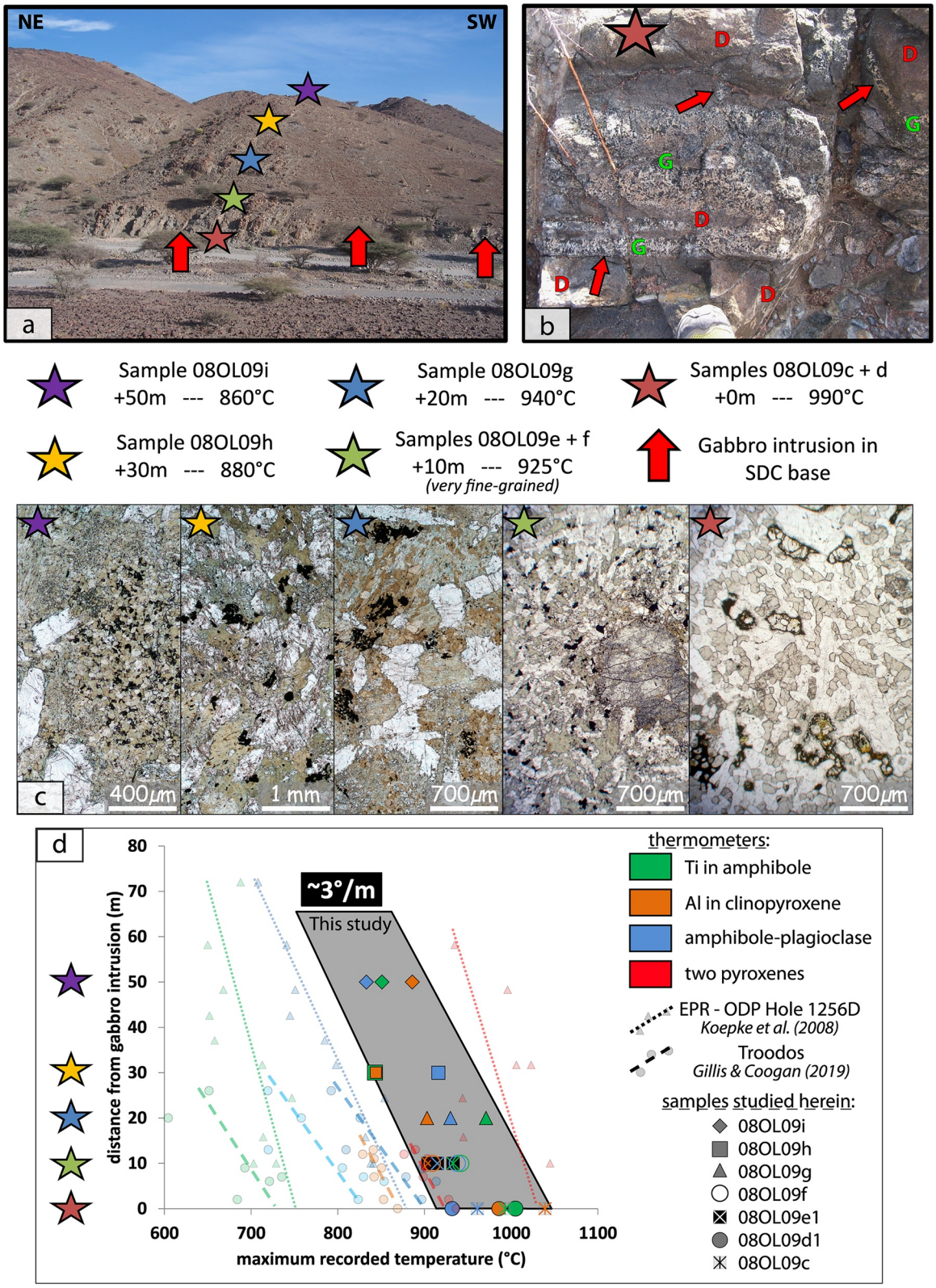
NE
SW
a
b
D
G
Sample 08OL09i
+50m --- 860°C
Sample 08OL09g
+20m --- 940°C
Samples 08OL09c + d
+0m --- 990°C
Sample 08OL09h
+30m --- 880°C
Samples 08OL09e + f
+10m --- 925°C
(very fine-grained)
Gabbro intrusion in
SDC base
c
400μm
1 mm
700μm
700μm
700μm
d
~3°/m
This study
distance from gabbro intrusion (m)
maximum recorded temperature (°C)
thermometers:
Ti in amphibole
Al in clinopyroxene
amphibole-plagioclase
two pyroxenes
EPR - ODP Hole 1256D
Koepke et al. (2008)
Troodos
Gillis & Coogan (2019)
samples studied herein:
08OL09i
08OL09h
08OL09g
08OL09f
08OL09e1
08OL09d1
08OL09c

gabbros) displays several facies with intergrowths of fine- and coarse-grained subophitic isotropic gabbros (Figure 4h), granular gabbros (Figure 4j), patchy gabbros (Figures 4i, 4k, and 4l) that are characterized either by cm felsic patches (Figure 4i), or by subophitic gabbros with large poikilitic clinopyroxenes and associated plagioclase chadacrysts (Figures 4k and 4l). Those various textural domains in the isotropic gabbro interval can usually be followed over tens of meters. Several gabbro in gabbro intrusive contacts are also present (Figures 4m, 4n, and 4o) and attest of various magma batch injections. Contacts are usually sutured, and locally underlined by felsic intrusions (Figures 4m and 4n). Similarly to the sections studied in MacLeod & Yaouancq (2000), and France et al. (2009), isolated foliated gabbro domains of few meters large are observed within the isotropic gabbro horizon (Figure 3); the foliation direction is parallel to the general direction defined by the underlying foliated gabbros and by the SDC. Deeper in the section, foliated gabbros are relatively homogeneous, and display granular textures (Figure 4g). The foliation in the foliated gabbros is generally parallel to the sub-vertical SDC orientation (trending ~140°N; Figures 3 and 4g).

A cross-section drawn along axis is presented in Figure 3. It has been drawn after a very careful mapping of the contact zones with the objective to track the presence of any potential fault for example close to the two SDC bodies that are mapped to the NW. There, no fault has been identified, and root zone outcrops with clear intrusive features are present, attesting of their normal position. To the SE, although gabbros are also clearly intrusive in the SDC root (e.g., Figures 7a and 7b; station 3 in Figure 3), it is possible that the large Wadi oriented WSW-ENE may underline a fault within the isotropic gabbro body (Figure 3). In any case, the structural data, and geological map presented herein, together with the numerous reported root zone outcrops attest to important depth variations of the SDC/gabbro transition when observed along axis (more than 150 m vertically on an along axis distance of ~150 m; Figure 3).

6. Key Petrological Features, and Estimates of Equilibrium Temperature

6.1. Dikes

Similarly to the other SDC/gabbro transitions studied in the Oman or Troodos ophiolites (France et al., 2009; Gillis, 2008; Gillis & Coogan, 2002, 2019; Gillis & Roberts, 1999), and at the East Pacific Rise (France et al., 2009, 2014; Gillis, 2008; Koepke et al., 2008; Wilson et al., 2006), the base of the SDC is recrystallized to hornfels-like granoblastic textures that are at odds with the classical doleritic textures of the basalts forming the SDC. In all studied areas granoblastic assemblages were interpreted as prograde metamorphic assemblages. Granoblastic textures observed herein are either widespread in the recrystallized dike (e.g., Figures 8a and 8b) or more commonly rather localized in granoblastic domains (e.g., Figure 7c purple and blue stars; Figures 8c and 8d). In the latter case, the initial igneous subophitic texture is preserved, and granoblastic domains are replacing larger pyroxene grains (e.g., Figures 8c and 8d). The granoblastic texture is more developed in finer grained dikes, and when moving closer to the intrusive gabbro body. All granoblastic samples studied in the Aswad area contain green to brown amphibole that is commonly organized as granoblastic amphibole patches (granoblastic grains are tens of μm wide, and related patches can be up to 1 mm wide; Figures 8c, 8d, 9). Granoblastic rocks described in crustal sections documenting the crust

Figure 7. Textural and temperature effect of magma injection at the base of the sheeted dike complex (station 3 in Figure 3). Red arrows in (a) point to the outcrops where gabbros have been observed intruding the sheeted dike complex base, and to the intrusive contact itself in (b). In (b) *G* highlight gabbros, and *D* dikes. Other samples have been collected in the sheeted dike complex at 10, 20, 30, and 50 m from the dike/gabbro contact (from red star). (c) Plane polarized light microscopic images of the various samples are presented to highlight their textural characteristics. In dikes samples localized at 50 and 20 m from the intrusive contact (purple, and blue stars, respectively), some 1–2 mm large patches of granoblastic brown amphiboles are present. In dike sample localized at 10 m from the intrusive contact (green star), a large clinopyroxene phenocryst has been preserved of the granoblastic overprint that is observed in the corresponding matrix. In dike sample localized at the intrusive contact (red star), olivine is present and the granoblastic overprint is well marked. (d) maximum temperature obtained for each sample with the various thermometers considered herein, where each thermometer is represented by a different color. An apparent temperature gradient (or metamorphic field gradient; gray box) of ~3°C.m^{-1} can be estimated from our data. Similar apparent temperature gradient estimates obtained by Gillis and Coogan (2019) in the Troodos ophiolite (dashed lines, and corresponding circles), and by Koepke et al. (2008) at ODP Hole 1256D (dotted lines, and corresponding triangles) are reported for comparison. Colors of points and of dashed-dotted lines document the used thermometer with red color for the two pyroxene thermometer (Andersen et al., 1993), green color for the Ti in amphibole thermometer (Ernst & Liu, 1998; values have been recalculated for the data from Gillis & Coogan, 2019 as those authors did not use this thermometer), orange color for the Al in clinopyroxene thermometer (France, Koepke, et al., 2010; values have been recalculated for the data from Gillis & Coogan, 2019 and Koepke et al., 2008 as those authors did not use this thermometer), and blue color for the amphibole-plagioclase thermometer (light blue corresponds to the raw estimates from Gillis & Coogan, 2019, when dark blue corresponds to their recalibrated values). See Section 4 for further details on the use of those thermometers. Corresponding data are presented in Table S2.

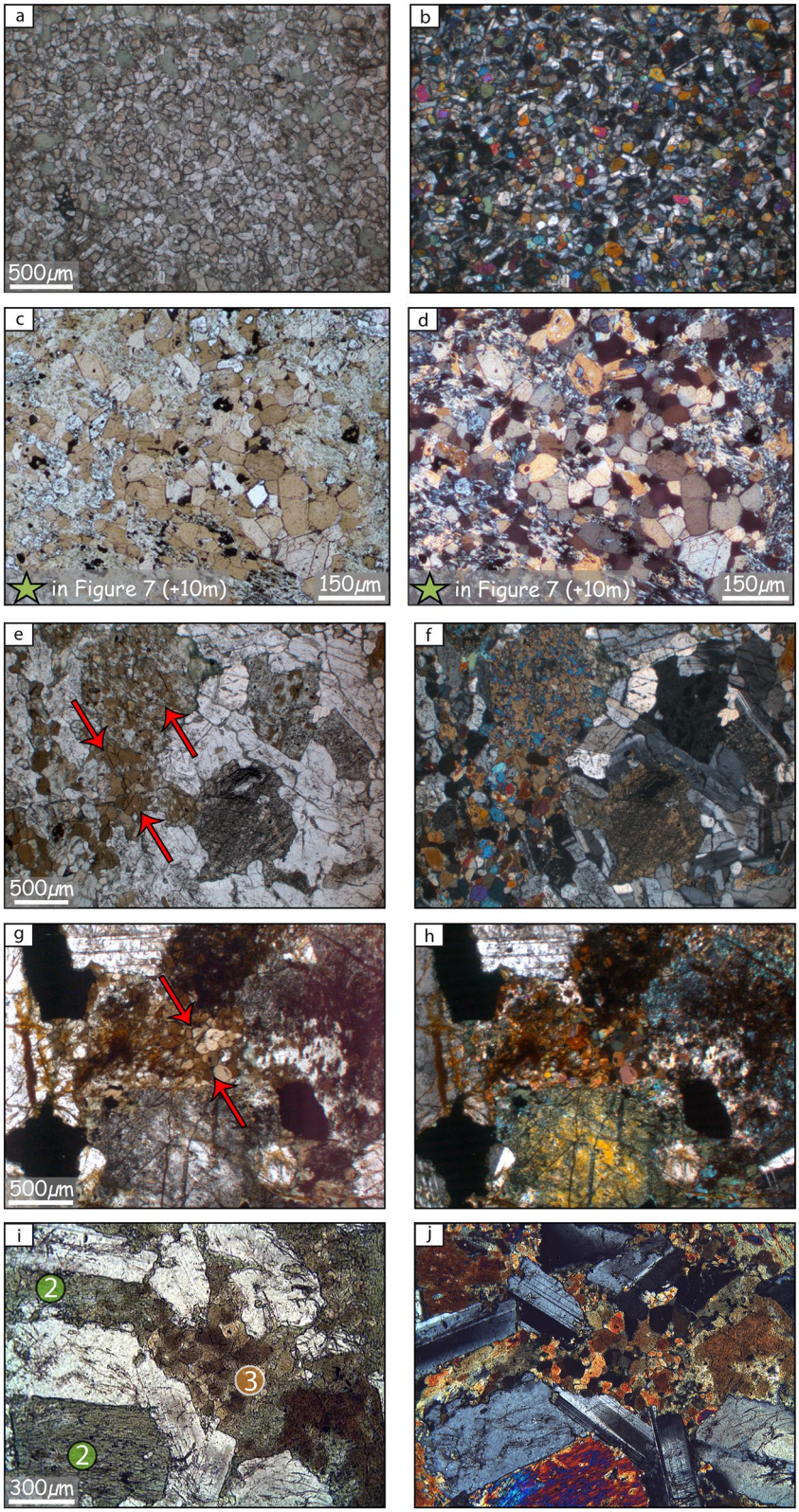
a
500μm
b
c
in Figure 7 (+10m)
150μm
d
in Figure 7 (+10m)
150μm
e
500μm
f
g
500μm
h
i
2
3
2
300μm
j

formed at fast-spreading centers contain both amphibole-bearing and amphibole-free domains (e.g., Gillis, 2008; Gillis & Coogan, 2019; Koepke et al., 2008). In contrast, granoblastic assemblages associated with dikes intruding gabbros at slow-spreading ridges are all amphibole-rich (Dick et al., 2019). The mineralogical assemblage of the recrystallized dikes studied herein includes plagioclase, clinopyroxene, amphibole, and Fe-Ti oxides (Ti-magnetite and/or ilmenite). Olivine is present in the granoblastic samples that are the closest to the contact with gabbros (e.g., present in most dikes in Figure 6, and in the deepest sample in Figure 7c red star). In order to track the textural evolution together with the evolution of the maximum temperature recorded in the reheated dikes at the SDC/gabbro transition, we have sampled a 50 m long profile above such a contact (site 3 in Figure 3; Figure 7). Samples at the very contact are strongly recrystallized and contain olivine in the mineralogical assemblage (red star in Figure 7c). At 10 m away from the contact (green star in Figure 7c), samples display well developed granoblastic texture (no olivine present from this level). Beyond 10 m from the contact granoblastic assemblages are only present locally in specific domains, and are characterized by assemblages containing granoblastic amphibole grains (e.g., Figure 7c purple and blue stars; Figures 8c and 8d).

6.2. Gabbros

Gabbros from the varitextured gabbro interval display subophitic to granular textures, and are intensely overprinted by hydrothermal fluids forming green to brown hornblende assemblages, actinolite-chlorite assemblages, and locally some prehnite-pumpellyite assemblages. Domains containing no plagioclase, and likely replacing large Fe-Mg minerals such as amphibole or pyroxene are composed of fine-grained granoblastic aggregates of brown amphibole (Figures 8e–8j). Pyroxene with brown amphibole rims or blebs are common, and transition from brown amphibole to green amphibole from core to rim is locally observed (e.g., Figure 10a). Prismatic green amphiboles are also locally recrystallized to brown amphibole granoblastic assemblages (e.g., Figure 10b). Gabbros locally contain some granoblastic patches that are remnants of dike pieces partially assimilated in the fossilized AML (see Figures 7c and 10d in France et al., 2009, and Figure 2c in Koepke et al., 2011 for related examples). An% of plagioclase in the isotropic gabbro studied herein are up to 75, and clinopyroxene Mg# up to 79 (Tables S1–S5).

6.3. Temperature Estimates

Following the numerous studies in which temperature estimates were performed at the SDC/gabbro transition (e.g., France et al., 2009; Gillis, 2008; Gillis & Coogan, 2019; Koepke et al., 2008), we have here selected very specific field stations to provide additional constraints of equilibrium temperatures (see Section 2.3). The followed approach and the various thermometers that are used herein are presented in Section 4. Values to be kept in mind while considering the temperature estimates presented in this study are the hydrous solidus temperature of hydrothermally altered dikes that is ~850°C (Erdmann et al., 2015; France, Koepke, et al., 2010), and the maximum temperatures that were recorded in previous studies in granoblastic rocks (1,045°C in ODP Hole 1256D by Koepke et al., 2008; 1,025°C in the Oman ophiolite by France et al., 2009; 1,020°C in the Troodos ophiolite by Gillis & Roberts, 1999). In the present study, we can follow the evolution of the maximum recorded temperatures estimated with increasing distance up section from the SDC/gabbro transition (Figure 7d). Our results highlight that the maximum recorded temperature is decreasing up section from the contact (maximum temperatures up to 1,040°C) to less recrystallized dikes at 50 m from the contact (maximum temperatures < 900°C; Figure 7d). This corresponds to an apparent temperature gradient of ~3°C.m^{-1} which is in the same order of magnitude as the apparent T gradient obtained by Koepke

Figure 8. Photomicrographs of recrystallized dikes (a–d) and gabbros (e–j) observed in plane-polarized light (a, c, e, g, and i), and cross-polarized light (b, d, f, h, and j). (a and b) display a dike sample (07OL54a) with a widespread granoblastic texture overprint (mineral assemblage composed of plagioclase, clinopyroxene, light pink orthopyroxene, and greenish chlorite-actinolite assemblages), when (c and d) display a dike sample (08OL09f) with localized amphibole-bearing granoblastic assemblages (see also Figure 7c purple & blue star, 9a for similar features); in (c) clinopyroxenes are containing tiny oxides, and greenish minerals are chlorite-actinolite assemblages. In gabbros, recrystallized features are also highlighted by recrystallized domains composed of granoblastic assemblages of amphibole (e–j). Depending on the samples granoblastic amphibole domains are associated either with nonrecrystallized clinopyroxene-plagioclase (e–h), or only with amphibole-plagioclase (i–j) suggesting that in those sample an initial alteration of clinopyroxene to amphibole may be required to record the granoblastic stage. Red arrows indicate some of the granoblastic domains in gabbros, and numbers in (i) refer to Figure 10 (samples in e and f: 07OL47b, g and h: 07OL57a, i and j: 08OC06).

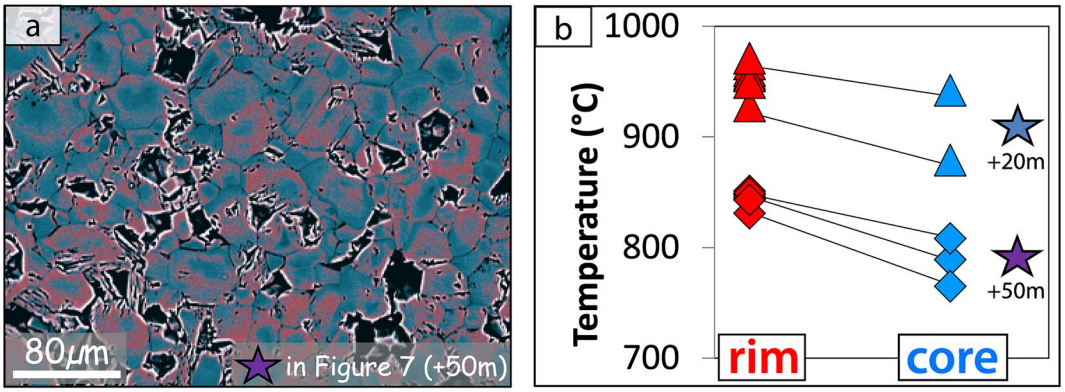

Figure 9. Granoblastic patch of brown amphibole showing chemical zonation in a recrystallized dike from Figure 7, and corresponding temperature estimates by using the Ti in amphibole thermometer (Ernst & Liu, 1998; see Section 4 for further details on the use of this thermometer). Amphibole grains are chemically zoned (a) with Ti-rich rims (red) in comparison to corresponding cores (blue) that documents the reheating stage (b); mineral rims document higher temperatures than corresponding mineral cores. Sample in colored backscattered image in (a) is 08OL9i (purple star in Figure 7; 50 m from the contact); in (b) triangles correspond to sample 08OL09g (blue star in Figure 7; 20 m from the contact), and diamonds correspond to sample 08OL9i (purple star in Figure 7; 50 m from the contact). Corresponding data are presented in Table S3.

et al. (2008) in ODP Hole 1256D (~3°C.m^{-1}), and by Gillis and Coogan (2019) in the Troodos ophiolite (~4°C.m^{-1}). This temperature gradient is here considered *apparent* as it records the maximum temperature reached at each point of the contact metamorphism aureole, but none of these maximum temperatures were reached at the same time as heat transfer by diffusion takes time. The temperature gradient is thus only apparent, has never existed as a real geothermal gradient in the history of the SDC/gabbro transition, and although it has been done in literature (e.g., Gillis, 2008; Gillis & Coogan, 2019; Koepke et al., 2008) it should not be used to calculate instant heat fluxes to be compared with active vent fields. The reheating stage is recorded in those dikes by, as an example, the inverse zoning of the granoblastic amphibole grains that compose some of the granoblastic assemblages (Figure 9). There the amphibole rims record temperature estimates that are ~50°C higher than their corresponding cores. Redox estimates in the 50 m above the intrusive contact documents conditions ranging from $\Delta FMQ = -1$ to +3 with no systematic variation with depth (redox estimates based on the oxybarometers of France, Ildefonse, et al., 2010, and of Sauerzapf et al., 2008). This corresponds to more reducing conditions than those estimated for granoblastic rocks at ODP Hole 1256D by Koepke et al. (2008). The maximum temperature estimates obtained on the dikes from the root zone outcrop presented in Figure 6 are in agreement with those obtained at the SDC/gabbro contact in Figure 7 as these are up to 1,020°C. Maximum temperature estimates using the Al in clinopyroxene thermometer of France, Koepke, et al. (2010) only document temperatures >940°C in the granoblastic samples that are located at the very contact with gabbros (e.g., in the root zone outcrop where dikes and gabbros are mutually intrusive in Figure 6, or at the very contact "0 meters" in Figure 7d). Those granoblastic samples are the only ones that contain olivine, demonstrating the accuracy of the comparison with France, Koepke, et al. (2010) experimental study, which showed that this mineral is only present in the reheating experiments ≥940°C. Equilibrium redox condition estimates for the dikes of this root zone outcrop document average values of $\Delta FMQ = +1.5$ (based on the oxybarometer of France, Ildefonse, et al., 2010).

Maximum temperature estimates in the gabbros from the root zone outcrop are up to 1,000°C, thus very similar to those obtained on the dikes, indicating that both lithologies where equilibrated in the same conditions during the overall reheating event (Figure 6). Corresponding redox estimates are of $FMQ = +1.2$ (based on the oxybarometer of France, Ildefonse, et al., 2010), thus similar to values obtained for the dikes when considering the uncertainty of the used oxybarometer that is of ~1 Log unit. Beside the textural evidences for gabbro reheating, temperature estimates also highlight the reheating stage, and allow us to determine for the first time the range of this reheating stage (Figure 10c). Large brown hornblendes, possibly documenting magmatic amphiboles, record temperatures of ~1,000°C, while their green hornblende rims correspond to temperatures of 600°C–700°C, showing conditions related to hydrothermal cooling

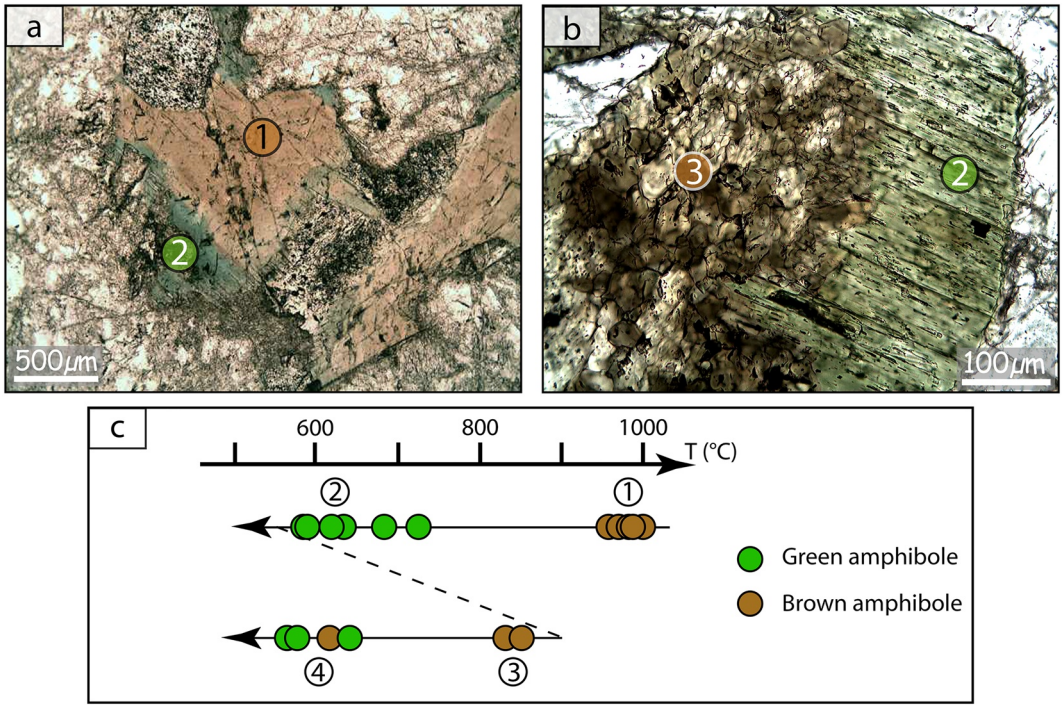

Figure 10. Recrystallization features and corresponding temperature estimates in isotropic gabbros (station 2 in Figure 3). Temperature estimates are performed by using the Ti in amphibole thermometer (Ernst & Liu, 1998; see Section 4 for further details on the use of this thermometer). (a) Large brown amphibole (*stage 1* hornblendes) of possibly magmatic origin records hydrothermal cooling and display green amphibole rims (*stage 2* hornblendes). (b) In some isotropic gabbros, green amphiboles (*stage 2* hornblendes) are locally recrystallized to brown amphibole granoblastic assemblages (*stage 3* hornblendes). (c) Temperature evolution during the evolution of a reheated isotropic gabbro (sample 08OC06, station 2 in Figure 3): *stage 1* amphiboles record temperatures up to 1,000°C, when *stage 2* amphiboles record temperatures down to 600°C. The reheating stage is locally documented with *stage 2* amphiboles that are recrystallized to *stage 3* granoblastic amphibole assemblages recording temperatures up to 850°C. The latter are locally re-equilibrated at lower temperature (*stage 4* hornblendes to actinolites). Transition from *stage 2* amphiboles to *stage 3* ones documents a reheating stage of >200°C. Corresponding data are presented in Table S4.

of the gabbros (Figures 10a and 10c). In some samples, green hornblendes are locally recrystallized to brown-hornblende granoblastic assemblages that record temperatures as high as 855°C, while the rims of some of those granoblastic grains eventually record temperatures of ~600°C (Figures 10b and 10c). This key result shows that some gabbros were hydrothermally cooled in a higher green-schist facies conditions before being reheated of more than 200°C.

7. Discussion

The new results presented herein were obtained to tackle specific open questions on the organization and evolution of the SDC/gabbro transition, and the interactions between the hydrothermal and magmatic systems. Hereafter, we first discuss the implications of our results on the quantification of the depth variations of the SDC/gabbro transition at oceanic spreading centers (Section 7.1), before discussing the evidences for successive melt injections and quantifying the related reheating events in dikes and gabbros at the AML level (Section 7.2). The comparison of these new results with literature data allow to present a much more detailed insight into the magmatic/metamorphic processes at the SDC/gabbro transition at fast spreading oceanic centers (Section 7.2). Together with thermometric estimates they are used to discuss the apparent thermal gradient that is recorded at the SDC base, to build simple thermo-kinetics models of the magma reservoir roof zone, and to discuss related heat fluxes and their link with active hydrothermal vents on the seafloor (Section 7.3). We then discuss the fate of the AML and the origin of the isotropic gabbro interval, before discussing the origin of the hydrothermal component that is recorded in MORBs at fast-spreading oceanic centers (Section 7.4).

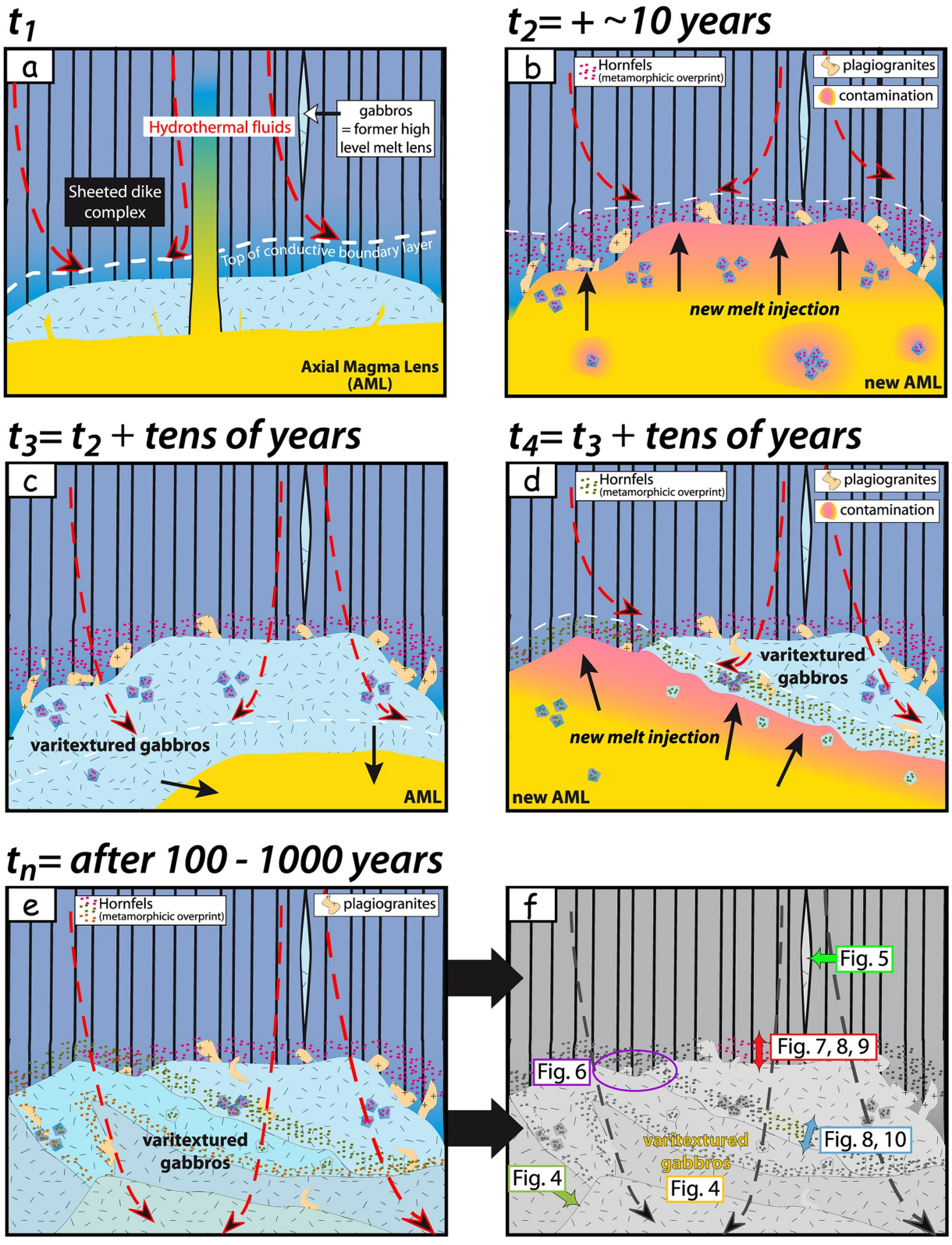
t1
a
Hydrothermal fluids
gabbros
= former high
level melt lens
Sheeted dike
complex
Top of conductive boundary layer
Axial Magma Lens
(AML)
t2= + ~10 years
b
Hornfels
(metamorphicic overprint)
plagiogranites
contamination
new melt injection
new AML
t3= t2 + tens of years
c
varitextured gabbros
AML
t4= t3 + tens of years
d
Hornfels
(metamorphicic overprint)
plagiogranites
contamination
varitextured
gabbros
new melt injection
new AML
tn= after 100 - 1000 years
e
Hornfels
(metamorphicic overprint)
plagiogranites
varitextured
gabbros
f
Fig. 5
Fig. 7, 8, 9
Fig. 6
Fig. 8, 10
varitextured
gabbros
Fig. 4
Fig. 4

7.1. Depth Variations of the Dike/Gabbro Transition in the Field

Seismic data from fast-spreading oceanic ridges have shown that the depth of the AML can vary vertically over hundreds of meters, over some kilometers along axis (e.g., Carbotte et al., 2013; Hooft et al., 1997; Marjanovic et al., 2018). In the oceanic crust this AML is likely represented by the upper isotropic gabbro level that fossilizes at the last stages of its evolution (e.g., France et al., 2009; Hayman et al., 2019; Koepke et al., 2011; MacLeod & Yaouancq, 2000; T. Müller et al., 2017). Deciphering whether the thickness of the isotropic gabbro level is representative of the original AML thickness is not trivial; nevertheless it is clear that the intrusive SDC/gabbro contact (e.g., Figures 4b–4f) is representative of the depth of the ultimate shallowest AML roof. Our new results highlight for the first time in fossil oceanic crust that depth variations of this SDC/gabbro contact can occur over more than 150 m vertically along the axis over a distance of ∼150 m (Figure 3). Our results also demonstrate that in a given section of a ridge, the depth level of a given magma lens may vary in time as remnants of former magma lenses are observed at >200 m above the highest intrusive contact between SDC and gabbro (Figure 5). The corresponding remnant of this former high level AML is represented by gabbro screens that were later on intruded by numerous dikes forming the present day SDC (Figure 5). The gabbro screen presented in Figure 5 contains some microgranular enclaves, implying that granoblastic dikes once located in the roof of this former high level AML have been stopped into the magma lens. This high level AML finally crystallized to form the observed enclave-bearing gabbros. All those field results imply that the AML depth could be highly variable both along axis, but also at a given locality on the ridge. Those depth variations are consistent with the results from seismic studies (e.g., Carbotte et al., 2013), and are likely related to the injection of new magma batches (replenishments), and could be either related to along axis variations of the melt supply, or to heterogeneous or cyclic melt supply at the top of a mushy lower crustal reservoir.

7.2. Melt Injections and Reheating Episodes in Dikes and Gabbros: Toward an Integrated Model

Previous field, structural, petrological, and geothermometric data on the SDC/gabbro transitions have highlighted that the top of the AML is usually intrusive in the SDC root zone that is reheated as attested by its characteristic granoblastic overprint (e.g., Coogan et al., 2003; France et al., 2009, 2014; France, Koepke, et al., 2010; Gillis, 2002, 2008; Gillis & Coogan, 2019; Gillis & Roberts, 1999; Koepke et al., 2008; Wilson et al., 2006). Here beside similar evidences for melt intrusion in the SDC root zone (Figures 4b–4f, 6a–6b, and 7), and related reheating events (Figures 7 and 9), we also show that several intrusive contacts have been observed where one gabbro is intruding another gabbro (Figures 4m–4o). Those intrusive relations document contacts between gabbroic bodies with various textures that record various magma batches (Figures 4h–4l). Given the numerous gabbro in gabbro intrusive contacts identified in the investigated area, together with the numerous root zone outcrops that we mapped (e.g., Figures 3, 4, and 6) it is clear that cyclic

Figure 11. General schematic model for the dynamics at the sheeted dike complex (SDC)/gabbro transition based on the results of this study, following France et al. (2009). (a) Initial situation presented in stage (a) corresponds to a stage after a magma injection, at that stage a dike is injected from the AML into the SDC; hydrothermal system cools down the series, and a conducting boundary layer is present between the base of the hydrothermal convecting cells and the top of the magma lens. A screen of isotropic gabbros is also represented and accounts for a former high level of the AML that had crystallized to form those gabbros that were subsequently intruded by the numerous dikes (e.g., Figure 5). Stage (b) corresponds to a recharge stage or to the injection of a new magma batch at the SDC base (Figures 4b–4f, 6a, 6b, 6d, 7). This triggers assimilation (and potential associated contamination; see Section 7.4), reheating of the dike root (and potential related anatexis and oceanic plagiogranite formation; Figure 4e) and corresponding recrystallization to hornfels like dikes (or granoblastic dikes; Figures 7, 8a–8f, and 9). Stage (c) during a magma-starved phase the previously intruded melt crystallizes to isotropic gabbro (or varitextured gabbros; Figures 4h–4l). Hydrothermal circulation affects the isotropic gabbros down to the top of the conductive boundary layer (dashed white line). Stage (d) corresponds to the injection of a new magma batch at the SDC/gabbro transition; intrusion affects both the and the partially (to fully) crystallized magma lens (Figures 4m–4o and 6). Gabbros can thus be reheated, recrystallized, and potentially assimilated (Figures 8g–8l and 10). Final stage (e) documents the final state of the SDC/gabbro transition where several magma injections are recorded. Numerous of those magma injections were associated with reheating and recrystallization of the intruded dikes and gabbros. Locally reheating features are not present and may account for intrusive events close to each other in time; in that case fresh magma is intruded in a mush. Figure (f) summarizes the Figures of the present study that documents each of the sketched results. Timescale estimates are from thermo-kinetic models (e.g., Fontaine et al., 2011, and our model presented in Figures 12 and 13 and related text), and from seismic observations performed at active ridges (see discussion for further details). Key observations related to timescales are (*i*) that it takes tens of years to crystallize a tens of meters thick magma lens (Figures 12 and 13; Fontaine et al., 2011), (*ii*). that tens of years are required to account for the reheating at the SDC base (Figure 12), (*iii*). that AML properties are potentially modified after seafloor eruptive events (e.g., Carton et al., 2008; Marjanovic et al., 2014), (*iv*). that melt-rich AML are common at fast-spreading ridges (Marjanovic et al., 2015; Singh et al., 1998), and *v*. that paleo spreading rates in Oman, and classical full spreading rate at a fast-spreading oceanic center are on the order on 10 $cm.y^{-1}$ (e.g., R. D. Müller et al., 2008; Rioux et al., 2012).

magma batches injection was the rule and widespread at the AML level. Clear petrologic reheating features are also observed in some gabbros (Figures 8e–8j and 10), demonstrating that a melt batch intrusion in gabbroic lithologies has the potential to affect texturally, mineralogically, and chemically the plutonic host. This conclusion was also reached in the Northern Oman ophiolite (France et al., 2013). The ~200°C reheating range shown in Figure 10c also emphasizes that melt injection at the AML level is not continuous but rather cyclic, since gabbros once intruded, could have experienced hydrothermal cooling down to ~600°C, before a new intrusion nearby occurred triggering a reheating event. This may correspond either to tens of years without injection for a 10 m thick intrusion (hundreds of years for a 60 m thick intrusion), or more likely to episodes with slightly deeper or laterally distant intrusions (see Section 7.4 for a discussion on the thermal effect of various sized intrusions).

Those results imply that the AML should not be considered as a permanent or steady state feature but rather as a transient one, and that melt supply at the AML level is cyclic rather than continuous. Cyclic or episodic melt injections may allow the AML to partially or fully crystallize under the influence of the overlying hydrothermal cooling system. In the absence of a phase of reinjection or replenishment, AML crystallization would take place within years to decades according to Fontaine et al. (2011). Similar cooling timescales were determined by using diffusion chronometry in the granoblastic roof rocks of such AMLs (Zhang et al., 2014), supporting the theoretical thermal models of Fontaine et al. (2011). Altogether those results are also consistent with seismic results at fast spreading ridges that indicate first that most of the reflectors document crystal-rich or mushy lenses (e.g., Singh et al., 1998), and second that seismic properties of the AML can vary at the decade timescale (e.g., Carton et al., 2008; Marjanovic et al., 2014). This new perspective for the evolution of the AML at fast spreading ridges suggests that former models involving a permanent or steady state AML that can move up/down or inflate/deflate (e.g., Coogan et al., 2003; France et al., 2009, 2014; France, Koepke, et al., 2010; Gillis, 2008; Koepke et al., 2008) should be replaced by models involving cyclic transient magma lenses injections close to the SDC/gabbro transition (Figure 11). Those injections intrude either the SDC root zone or the isotropic gabbro level, trigger reheating of host rock (or host mush), and possibly partial assimilation. Those injections may or may not be associated with dike injection, and possibly with seafloor eruption. Subsequently the intruded magma likely crystallizes to form the isotropic gabbro interval in tens of years (e.g., Fontaine et al., 2011), while a new magma batch intrudes either in the SDC root zone, or in its underlying partially to fully crystallized varitextured gabbro level (Figure 11).

7.3. Intrusion Size, Geothermal Gradients, Heat Fluxes, and Relation With Active Hydrothermal Vents

The apparent temperature gradient (3°C.m^{-1}) that is highlighted by the maximum temperature recorded at the base of the SDC corresponds to a metamorphic field gradient (Figure 7d). It was never active as a geothermal gradient as the maximum temperatures obtained at the various depths were reached at various times (Figures 12a and 12b). Similar apparent temperature gradients were obtained at ODP Hole 1256D that formed at the East Pacific Rise (3°C.m^{-1}; Koepke et al., 2008; Figure 7d), and in the Troodos ophiolite (4°C.m^{-1}; Gillis & Coogan, 2019; Figure 7d). In order to better quantify this reheating stage, and to reproduce the thermal constraints we obtained with geothermometers, we have conducted simple conductive thermo-kinetic models to test the effect of the intrusion of a magma body at the base of the SDC. Key questions to be approached with those models are (1) What are the temperature and size of the gabbroic intrusion required to trigger the apparent thermal gradient? (2) What is the lifespan of the gabbroic intrusions? (3) What is the duration required to produce the apparent temperature gradient (or metamorphic field gradient)? (4) What are the real geothermal gradients, how do they evolve with time, and to what range of heat fluxes do those correspond? (5) Are those heat fluxes compatible with the heat fluxes estimated at active hydrothermal vent fields, and what are their potential lifetimes?

We have used a transcription for PC of the CONTACT program (Peacock, 1989; Spear, 1989, 1991; Spear & Peacock, 1990) that simulates contact metamorphism by using an explicit finite difference algorithm to solve the one-dimensional heat transfer from an intrusion to the intruded host rock. In the model we assume that the igneous body is instantaneously intruded, and that heat transfers in the magma only proceeds by conduction. Furthermore, we do not consider potential heat transfers from the underlying magma reservoir that proceeds over longer timescales. Thermodynamic constants have been selected following Cannat

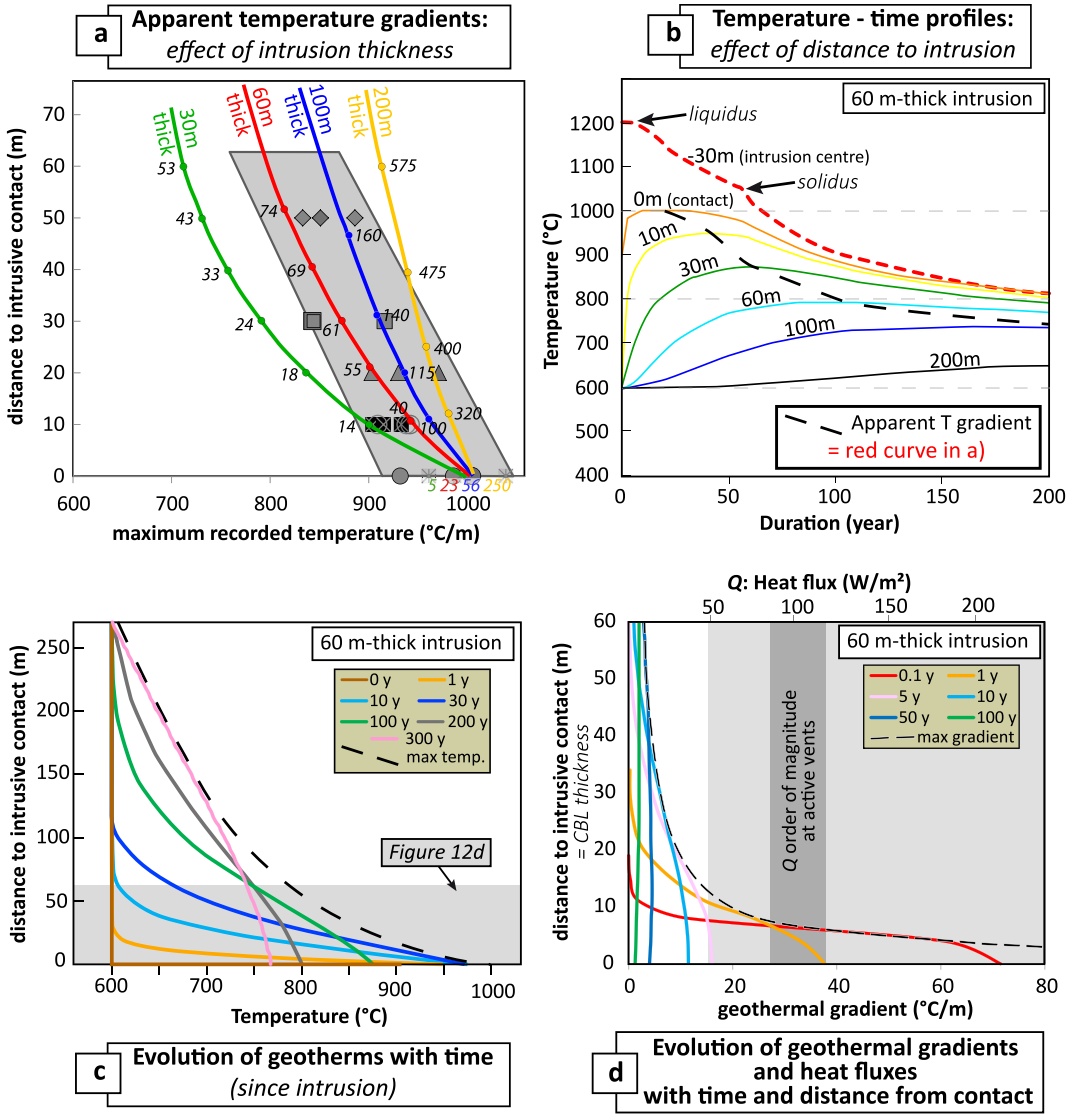

Figure 12. Results of the thermo-kinetic model performed herein (see Section 7.3 for further details on the model). (a) Modeled apparent temperature gradients (= field metamorphic gradients; 4 colored curves), compared with the natural apparent temperature gradients obtained herein (all natural data are summarized in Figure 7, and are presented here in gray colors). In panel (a) the effect of the intruded magma lens thickness on the apparent temperature gradient is tested. The data obtained in the present study (gray box) are best reproduced by intrusions of 60–100 m thick. Intruding melt temperature has been set to 1,200°C to account for the temperature recorded in the dikes at the very contact (~1,000°C). The apparent temperature gradient is the record of the highest temperature reached at increasing distance from the intrusive contact, and corresponds to the gradient that is recorded by the studied rocks. Heat being extracted by conduction, the duration required to reach the maximum temperature at various distances from the contact is different on each point (see Figures 12b and 12c). This duration (in years) is documented in (a) by the numbers written on the 4 modeled curves at various depths. Panel (b) modeled evolution of temperature with time at various points of the studied profile in the case of a 60 m thick intrusive body. The dashed red curve represents the thermal evolution at the center of the intrusion (−30 m); other curves labeled with positive distances (0, 10, 30, 60, 200 m) document temperature evolution in the SDC, at various distances from the contact. It is clear from (b) that the maximum temperatures reached at various distance from the contact are obtained at various times, highlighting why temperature gradients that document the maximum reached temperatures in (a) are only apparent and did not exist at a given time. Panel (c) modeled evolution of geotherms with time in the case of a 60 m thick intrusive body. Geotherms are the evolution of temperature with increasing distance from the contact at a given time. The maximum temperature recorded at a given depth during the overall evolution of the system is highlighted by the dashed black curve ("max temp.") and corresponds to the apparent temperature gradient presented in Figure 12a (red curve for a 60 m thick intrusion. Panel (d) Evolution of geothermal gradients (bottom *x*-axis) and heat fluxes (top *x*-axis) with time (color) and distance from contact (*y*-axis) in the case of a 60 m thick intrusive body. Geothermal gradients are the slopes of the curves presented in (c). Also documented is the order of magnitude of the heat flux (Q) at very active hydrothermal vents (gray fields; e.g., Lowell et al., 2013). The dashed curve highlights the maximum geothermal gradient that has been experienced at each depth of the profile, and the thickness of the conductive boundary layer that has been affected by a given geothermal gradient. It is clear from (d) that the 3°C.m^{-1} value obtained for the apparent temperature gradient in Figure 7d can neither be used as a proxy for geothermal gradient, nor in discussions aiming at comparing geothermal gradients to heat fluxes at active vents as it has been sometimes done in previous studies.

et al. (2004), Gillis and Coogan (2019), Lesher and Spera (2015), Spear and Peacock (1990) with a thermal conductivity of 3.0 W/m/K, a rock density of 3,000 kg/m^3, a specific capacity of 1,200 J/kg/K , a latent heat of crystallization of 400 kJ/kg. When considering the equilibrium temperatures obtained from geothermometers at the gabbro/dike contact (1,000°C–1,040°C), models show that the intruding melt temperature should be of at least 1,200°C, casting for a relatively primitive basaltic melt. We thus set the liquidus at 1,200°C, and an almost dry solidus around 1,050°C. A temperature of 600°C was chosen to account for the far field steady state temperature that likely corresponds to the high hydrothermal temperatures recorded in the dike section (e.g., Alt et al., 2010), and that is consistent with the lowest temperatures we obtained and that preceded the reheating stage (point 2 in Figure 10c). Models considering various intrusion thicknesses have been tested, and results indicate that 60–100 m thick intrusive bodies are the most likely to reproduce the apparent temperature gradient (Figure 12a). This is consistent with our field results showing that relatively homogeneous gabbroic bodies can be followed on thicknesses of tens of meters, or with the thickness of the isotropic gabbro level that was drilled at IODP Hole 1256D (e.g., Wilson et al., 2006). Those results show that a single intrusion of 60–100 m can account for the measured apparent temperature gradient, but does not rule out potential reinjections in a smaller igneous body, or multiple injections of smaller bodies. In the following we will consider the case of a single 60 m thick intrusion. The corresponding model highlights that the 60 m thick intrusion solidifies after ∼60 years (Figure 12b). The durations to reach the maximum temperatures that are recorded by the rocks at the various depths of the apparent temperature gradient are increasing up section while moving away from the intrusive contact; those are of ∼23 years at the contact, and of 61 and 74 years at 30 and 50 m from the contact, respectively (Figures 12a and 12b). It also takes hundreds of years to fully cool down the system to 600°C (Figure 12b). Real instantaneous geothermal gradients can also be extracted from the model; they are transient features that quickly evolve with time (Figures 12c and 12d). As expected for any contact metamorphism episode highest geothermal gradients are observed on short distances from the intrusive contact, immediately after the intrusion time, and rapidly decrease (Figure 12d). As an example geothermal gradients of tens of degrees per meter are recorded just after the intrusion and affect 5–10 m of the overlying conductive boundary layer; geothermal gradients of >25°C/m are present on ∼10 m one year after the intrusion (Figure 12d). Durations >10 years will produce geothermal gradients that will be <10°C/m (Figure 12d). Once geothermal gradients (dT/dz) are identified, corresponding heat flux (Q) can be calculated and eventually compared to heat fluxes released at active hydrothermal vents on the seafloor. Q is obtained following Fourier's law, such that $Q = -K\,(dT/dz)$ where K is the thermal conductivity (here taken as 3 W/m/K). Corresponding heat fluxes are for example of 210, 75, 30 W/m^2 for geothermal gradients of 70, 25, and 10°C/m, respectively (Figure 12d). Heat fluxes required to feed an active vigorous black smoker system have been estimated by seafloor heat flow studies and corresponding models, and are on the order of ∼100 W/m^2, an order of magnitude perfectly fitting to our results of the first decade following magma injection (Figure 12d; e.g., Lowell et al., 2013). Lowell et al. (2013) additionally showed that the thickness of the conductive boundary layer affected by such high geothermal gradients should be on the order of 10 m, perfectly matching our estimates (Figure 12d). Furthermore our results provide constraints on the duration of such transient high geothermal gradients with heat fluxes >30 W/m^2 that could not be sustained for more than ∼10 years (Figure 12d). Such short durations are consistent with Humphris and Cann (2000) conclusions, and are also consistent with the rapid changes that are observed at fast-spreading ridges active hydrothermal vents following magmatic events (e.g., Lilley et al., 2003). The stability of relatively lower heat fluxes (e.g., 18 MW that corresponds to 18 W/m^2 if we consider a 1 km long and 1 km wide AML) that has been observed over 26 months at the Juan de Fuca Ridge (Xu, Jackson, et al., 2014) is also consistent with our models but would not be stable over more than tens of years (Figure 12d). The estimates associated with the models presented above are associated with large uncertainties that cannot be assessed in details herein, but Lowell et al. (2013) noted as an example that heat output values are uncertain by a factor of two, and should thus rather be considered as documenting the order of magnitude of this parameter.

7.4. Fate of the AML, Assimilation, and MORB Contamination

The fate of the AML itself remains controversial and its fossilization to form the upper isotropic gabbros interval (e.g., Coogan et al., 2002; France et al., 2009; Koepke et al., 2011; MacLeod & Yaouancq, 2000) is

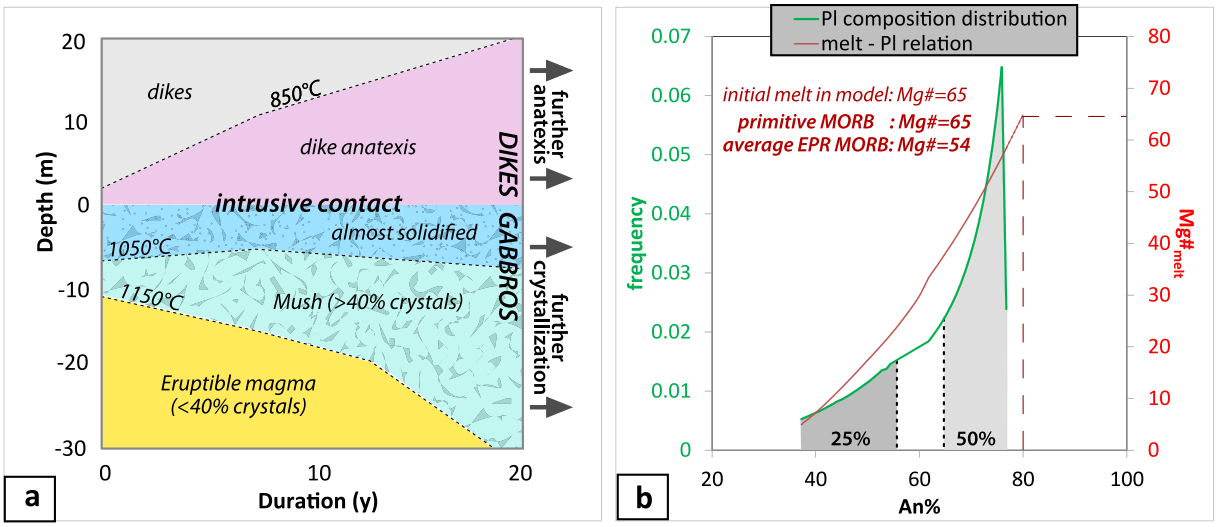

Figure 13. Thermo-kinetic & thermodynamic models of the dike/gabbro transition. Thermo-kinetic models are associated to those presented in Figure 12 and in related Section 7.3; thermodynamic model is based on Rhyolite-MELTS (Gualda et al., 2012), and is presented in Section 7.4. (a) displays the depth (in meters) evolution of isotherms in both dikes (depths >0 m) and solidifying gabbros (depths <0 m) with time (in years) following a basaltic melt intrusion event (1,200°C) at $t = 0$. Also documented in pink is the domain of the SDC that is equilibrated at a temperature >850°C that corresponds to the domain where hydrous anatexis is possible as the solidus temperature of hydrothermally altered dike is ~850°C (France, Koepke, et al., 2010). MELTS models are used to document the melt fraction in the crystallizing magma lens (bellow 0 m). Key observation is that the anatectic domain (pink) is never in contact with eruptible magma (yellow), and thus direct contamination is unlikely unless an additional process triggers a mixing event. (b) Thermodynamic fractional crystallization model tracking the evolution of plagioclase composition upon differentiation of a primitive MORB melt (initial melt has a Mg# = 65). The red curve links the instantaneous plagioclase composition to the one of the equilibrium melt (right vertical axis). The green histogram curve documents the distribution of plagioclase composition along the liquid line of descent of a primitive MORB melt in a closed system; results highlight that ~50% of the plagioclase grains have An%>65, and ~25% have An%<55. Plagioclase grains from the isotropic gabbro interval having a composition of An% = 80 are in equilibrium with relatively primitive MORB melts (Mg#>60; dashed curve). It should be noted that the magma - mush transition (when crystal content > 40% and that the magma becomes noneruptible) is at An%~65, meaning that the presence of Pl with An%<65 in erupted lavas is very unlikely. Average EPR MORB is from Rubin and Sinton (2007).

occasionally questioned (e.g., Lissenberg et al., 2019). The main issue is that the global average composition of the isotropic gabbro interval may be too evolved to fit the composition of both average and primitive MORBs (Lissenberg et al., 2019; Natland & Dick, 1996). Evolved felsic and oxide-rich rocks are commonly described among the various lithologies forming the isotropic gabbro interval along with evolved and primitive gabbroic domains (e.g., France et al., 2009; Koepke et al., 2011; MacLeod & Yaouancq, 2000; T. Müller et al., 2017; Natland & Dick, 1996; Zhang, Koepke, et al., 2017). An alternative model would be that the supposed evolved composition of this upper plutonic sequence would result from the extraction of reactive interstitial melt that would be extracted at the top of the underlying mushy magma reservoir (Lissenberg et al., 2019; Natland & Dick, 1996) similarly to what was recently observed at the scale of an igneous reservoir at a slow-spreading oceanic center (Boulanger et al., 2020). One way to solve this issue is to quantify the weighted average composition of the whole isotropic gabbro interval, a difficult exercise as most of the studied areas (e.g., ICDP OmanDP Hole GT3A, Hess Deep upper plutonic section, or ODP Hole 1256D) do not cover the full interval (from the dikes to the foliated gabbros), and cannot be used for such a calculation. Zhang, Koepke, et al. (2017) has indeed suggested that some evolved lithologies may be concentrated close to the roof of the AML, implying that any attempt of weighted average should really be performed on the full isotropic gabbro interval. The only estimate available to our knowledge was performed by MacLeod & Yaouancq (2000) who found that the bulk composition of this critical horizon is similar to average MORBs. Given the uncertainties associated with this estimate, this conclusion should nevertheless be considered with caution. The results of the thermo-kinetic model presented herein (Section 7.3; Figure 12) also supports that the isotropic gabbro interval crystallized from a relatively primitive basaltic melt. Indeed, our models highlight that the temperature of the intruding melt required to produce the observed apparent temperature gradient has to be ~1,200°C, an equilibrium temperature characteristic of primitive basaltic magmas. The huge geothermal gradients that are recorded at the SDC/gabbro contact (Figure 12)

also strongly suggest that any magma subject to such gradients would crystallize on site relatively quickly. This is evident when considering the thermal profiles within the intruded body that are complementary to the ones obtained for the intruded SDC base; these profiles show that at the time of intrusion several meters of the intruding body directly crystallize at the contact with the base of the SDC (Figure 13a). This rapid crystallization stage nevertheless proceeds at ~1,000°C (Figure 13a), and fast-growth features such as skeletal and dendritic crystals are expected in gabbros rather that chilled margins that would likely form at lower temperatures. Such specific minerals shapes are common in the isotropic gabbro interval (Kelemen et al., 2020; Koepke et al., 2011), and thus support our thermo-kinetic model results. Mineral compositions in the intruding gabbros also attest to the crystallization of relatively primitive MORB type melts. The least evolved plagioclase present in the gabbros studied in the Aswad area have An% up to 75, consistent with other data from the isotropic gabbro interval in Oman in which the highest An contents are between 70 and 80 (Coogan et al., 2002; MacLeod & Yaouancq, 2000; Müller et al., 2017), and with other data from the isotropic gabbro interval at ODP Hole 1256D in which the highest An contents reach 80 (Koepke et al., 2011). Thermodynamic models testing the crystallization of primitive MORB (Mg# = 65; 0.5% of water to account for the water rich content of the Oman ophiolite parental melts; MacLeod et al., 2013) by using Rhyolite-MELTS (Gualda et al., 2012) allow us to follow the evolution of plagioclase composition with melt composition and temperature (red curve, Figure 13b). Fractional crystallization results imply that the most primitive plagioclase grains that are present in the isotropic gabbro interval have crystallized from relatively primitive MORB melts (Mg# of the melt between 60 and 65) that were thus present at this level (Figure 13b). All those results clearly demonstrate that the isotropic gabbro interval initially crystallized from relatively primitive MORB-type melts, but it does not imply that the bulk composition of the interval is similar to that of primitive MORB. To advance the discussion on this topic, our thermodynamic model can be used to quantify the repartition of compositions along the liquid line of descent (green curve, Figure 13b). It shows that crystallizing a primitive MORB in a closed system would result in ~50% of the plagioclase grains with An%>65, and ~25% of the plagioclase grains with An%<55 (Figure 13b). Although a weighted average of the isotropic gabbro interval has not been conducted in the area studied herein, and it cannot be realized in sections were the full interval has not been recovered (e.g., ICDP OmanDP Hole GT3A, Hess Deep upper plutonic section, or ODP Hole 1256D), some specific observations can be used. One of the best examples is represented by the detailed petrology of the isotropic gabbros as they contain relatively primitive subophitic domains with An% usually >65, and granular domains with An% usually <55 (Koepke et al., 2011; Müller et al., 2017). Koepke et al. (2011) noticed that granular domains, which are locally heavily altered and underlined by whitish patches, form <30% of the isotropic gabbro interval, matching well the estimates extracted from our thermodynamic models presented above (~25% of plagioclase with An%<55). Furthermore constraints are clearly required to make progress on this subject, but any future attempt will require mass balances at the scale of the full interval in areas that allow for it, and will have to consider the effect of potential subsidence of primitive crystals (e.g., Coogan et al., 2002; Nicolas et al., 2009) and of hydrothermally altered rock assimilation (e.g., Coogan et al., 2003; Fischer et al., 2016; France et al., 2014; Michael & Cornell, 1998; Wanless et al., 2010).

MORB contamination at crustal levels has been inferred from basalt compositions (Chaussidon & Marty, 1995; Coogan et al., 2003; Fischer et al., 2016; Gannoun et al., 2007; Le Roux et al., 2006; Michael & Cornell, 1998; Wanless et al., 2011), and proposed to be related to the assimilation process that is observed in the field in SDC/gabbro transects of present day oceanic crust, and ophiolites (Coogan, 2003; Coogan et al., 2003; France et al., 2009, 2013, 2014; Gillis & Coogan, 2002; Hayman et al., 2019; Koepke et al., 2011). Although the contamination of the AML is established at depth based on those field results, the subsequent eruption of the contaminated melt filling the AML is unlikely. Indeed the assimilation process is endothermic, and thus triggers the partial crystallization of the assimilating magma lens (e.g., DePaolo, 1981), which thus turn to be a mush lens filled with crystal-rich noneruptible material (noneruptible when >40% of crystals are present; e.g., Lejeune & Richet, 1995). Alternatively, contamination may be achieved by mixing with anatectic melts produced by hydrous partial melting of previously altered sheeted dikes of the AML roof (plagiogranite-like; e.g., Coogan et al., 2003; Fischer et al., 2016; France et al., 2014; France, Koepke, et al., 2010). Nevertheless, although dike anatexis initiates at the time of melt intrusion, most of the anatectic stage develops later as it is related to the release of the latent heat of crystallization from the underlying gabbro body (Figure 13a). Also it is clear that intense crystallization occurs at the roof of any

newly injected magma batch immediately after the injection (blue in Figure 13a) preventing any interaction between the melt feeling the remaining magma lens (yellow in Figure 13a), and the area affected by anatexis (pink in Figure 13a). This result highlights that although assimilation does occur as identified in the field (e.g., Coogan et al., 2003; France et al., 2009), and anatexis of dikes or gabbros is likely (e.g., Gillis & Coogan, 2002; France et al., 2014; France, Koepke, et al., 2010; France, Ildefonse, et al., 2010; Koepke et al., 2004), the eruptible melt-rich areas of the AML, which essentially feed an eruption, remains isolated from those anatectic domains, and thus of any potential contamination (Figure 13a). MORB contamination being effectively identified in seafloor samples (e.g., Michael & Cornell, 1998), it follows that an alternative process, like magma mixing, should be involved. Such mixing could occur either when a new magma batch (or new magma lens) is emplaced in a contaminated area (anatectic domain at the SDC base, or partially crystallized gabbroic domain contaminated by hydrothermally altered dike assimilation), or while uncontaminated melt migrates through a contaminated area on its way to the surface. This makes such a contamination process more likely in very active ridge segments where melt reinjections are the rule, and rather rare in other segments.

8. Conclusion

We provide herein a detailed study of a section of the dike/gabbro transition in the Oman ophiolite, where igneous, metamorphic, and hydrothermal processes related to the AML dynamics are interacting. Main results are that:

- Depth variation of the dikes/gabbros transition are widespread, and can vary of up to 150 m in depth over distances of ∼150 m along axis. Depth variations with time are also recorded as remnants of high level AMLs are observed at hundreds of meters above the last dikes/gabbros transition level
- AMLs may not be permanent or steady state features at fast spreading centers, but rather transient ones that are associated with magma batch injections close to the dikes root zone
- Both dikes and gabbros are repeatedly intruded, and display reheating features. Intruded host is locally reheated of more than 200°C, up to >1,000°C, by basaltic melts that were equilibrated at ∼1,200°C
- Thermo-kinetic models suggest that intrusive bodies were tens of meters thick, and crystallized in tens of years, triggering the reheating and potential anatexis of the hydrothermally altered basaltic (or gabbroic) host. Models show that associated anatectic melts (plagiogranitic) are never in contact with the magma reservoir eruptible melt, and mixing events are thus required to account for the hydrothermal contamination that is often reported in MORBs
- Results of the thermo-kinetic models highlight that the crystallization of such tens of meters thick intrusive bodies produced heat fluxes at their roof that are similar to those measured at active high temperature hydrothermal vents (tens to hundreds of degrees centigrade per meter). The corresponding conductive boundary layer would be <10 m thick, and the related high heat fluxes would last for less than a decade
- The shallowest gabbros of the lower crustal section, the isotropic gabbro interval, have initially crystallized from relatively primitive MORB melts

Data Availability Statement

All analytical data used in this study are available at the OTELo Reasearch Data Repository (ORDaR - (https://doi.org/10.24396/ORDAR-54).

Acknowledgments
This study relies on field campaigns conducted thanks to the hospitality of the Omani people, and the Directory of Minerals at the Ministry of Commerce and Industry of the Sultanate of Oman. The authors thank Françoise Boudier for her help in the field, and for many discussions related to the root zone of the SDC. Adolphe Nicolas is also thanked for his help in the field, and several advices related to field work in the Oman ophiolite. Mathilde Cannat, Fabrice Fontaine, and Javier Escartin are thanked for discussions related to hydrothermal vents. This study greatly benefited from thorough reviews by Milena Marjanovic, an anonymous reviewer, the associate Editor, and the Editor, whom the authors gratefully thank. Christophe Nevado & Doriane Delmas are thanked for their high quality thin sections. This research was supported by the Région Lorraine ('soutien aux projets de recherche' program), and by CNRS-INSU program SYSTER, and IODP-France. This is CRPG contribution 2753. Open access funding enabled and organized by Projekt DEAL.

References

Abily, B., Ceuleneer, G., & Launeau, P. (2011). Synmagmatic normal faulting in the lower oceanic crust: Evidence from the Oman ophiolite. *Geology*, *39*(4), 391–394. https://doi.org/10.1130/g31652.1

Aghaei, O., Nedimović, M. R., Carton, H., Carbotte, S. M., Canales, J. P., & Mutter, J. C. (2014). Crustal thickness and Moho character of the fast-spreading East Pacific Rise from 9°42′N to 9°57′N from poststack-migrated 3-D MCS data. *Geochemistry, Geophysics, Geosystems*, *15*, 634–657. https://doi.org/10.1002/2013gc005069

Alt, J. C., Laverne, C., Coggon, R. M., Teagle, D. A. H., Banerjee, N. R., Morgan, S., et al. (2010). Subsurface structure of a submarine hydrothermal system in ocean crust formed at the East Pacific Rise, ODP/IODP Site 1256. *Geochemistry, Geophysics, Geosystems*, *11*, Q10010. https://doi.org/10.1029/2010gc003144

Andersen, D. J., Lindsley, D. H., & Davidson, P. M. (1993). QUILF: A pascal program to assess equilibria among Fe-Mg-Mn-Ti oxides, pyroxenes, olivine, and quartz. *Computers & Geosciences*, *19*(9), 1333–1350. https://doi.org/10.1016/0098-3004(93)90033-2

Barth, G. A., & Mutter, J. C. (1996). Variability in oceanic crustal thickness and structure: Multichannel seismic reflection results from the northern East Pacific Rise. *Journal of Geophysical Research*, *101*, 17951–17975. https://doi.org/10.1029/96jb00814

Boddupalli, B., & Canales, J. P. (2019). Distribution of crustal melt bodies at the hot spot-influenced section of the galápagos spreading centre from seismic reflection images. *Geophysical Research Letters*, *46*, 4664–4673. https://doi.org/10.1029/2019GL082201

Bosch, D., Jamais, M., Boudier, F., Nicolas, A., Dautria, J. M., & Agrinier, P. (2004). Deep and high-temperature hydrothermal circulation in the Oman ophiolite—Petrological and isotopic evidence. *Journal of Petrology*, *45*, 1181–1208. https://doi.org/10.1093/petrology/egh010

Boudier, F., Ceuleneer, G., & Nicolas, A. (1988). Shear zones, thrusts and related magmatism in the Oman ophiolite: Initiation of thrusting on an oceanic ridge. *Tectonophysics*, *151*, 275–296. https://doi.org/10.1016/0040-1951(88)90249-1

Boudier, F., & Nicolas, A. (2007). Comment on "dating the geologic history of Oman's Semail ophiolite: Insights from U-Pb geochronology" by C. J. Warren, R. R. Parrish, D. J. Waters and M. P. Searle. *Contributions to Mineralogy and Petrology*, *154*, 111–113. https://doi.org/10.1007/s00410-007-0189-5

Boudier, F., Nicolas, A., & Ildefonse, B. (1996). Magma chambers in the Oman ophiolite: Fed from the top and the bottom. *Earth and Planetary Science Letters*, *144*, 239–250. https://doi.org/10.1016/0012-821X(96)00167-7

Boulahanis, B., Carbotte, S. M., Huybers, P. J., Nedimović, M. R., Aghaei, O., Canales, J. P., & Langmuir, C. H. (2020). Do sea level variations influence mid-ocean ridge magma supply? A test using crustal thickness and bathymetry data from the East Pacific Rise. *Earth and Planetary Science Letters*, *535*, 116–121. https://doi.org/10.1016/j.epsl.2020.116121

Boulanger, M., France, L., Deans, J. R., Ferrando, C., Lissenberg, J., & von der Handt, A. (2020). Magma reservoir formation and evolution at a slow-spreading center (Atlantis Bank, Southwest Indian Ridge). *Frontiers in Earth Sciences*, *8*, 554598. https://doi.org/10.3389/feart.2020.554598

Canales, J. P., Detrick, R. S., Carbotte, S. M., Kent, G. M., Diebold, J. B., Harding, A., et al. (2005). Upper crustal structure and axial topography at intermediate spreading ridges: Seismic constraints from the Southern Juan de Fuca Ridge. *Journal of Geophysical Research*, *110*, B12104. https://doi.org/10.1029/2005JB003630

Canales, J. P., Detrick, R. S., Toomey, D. R., & Wilcock, W. S. D. (2003). Segment-scale variations in the crustal structure of 150-300 kyr old fast spreading oceanic crust (East Pacific Rise, 8°15′N-10°5′N) from wide-angle seismic refraction profiles. *Geophysical Journal International*, *152*, 766–794 https://doi.org/10.1046/j.1365-246X.2003.01885.x

Canales, J. P., Nedimović, M. R., Kent, G. M., Carbotte, S. M., & Detrick, R. S. (2009). Seismic reflection images of a near-axis melt sill within the lower crust at the Juan de Fuca Ridge. *Nature*, *460*(7251), 89–93. https://doi.org/10.1038/nature08095

Cannat, M., Cann, J., & Maclennan, J. (2004). Some hard rock constraints on the supply of heat to mid-ocean ridges. In C. R. German, J. Lin, & L. M. Parson (Eds.), *Mid-ocean ridges: Hydrothermal interactions between the lithosphere and oceans* (pp. 111–149). Washington, DC. American Geophysical.

Carbotte, S. M., Arnulf, A., Spiegelman, M., Lee, M., Harding, A., Kent, G., et al. (2020). Stacked sills forming a deep melt-mush feeder conduit beneath Axial Seamount. *Geology*, *48*(7), 693–697. https://doi.org/10.1130/g47223.1

Carbotte, S. M., Detrick, R. S., Harding, A., Canales, J. P., Babcock, J., Kent, G., et al. (2006). Rift topography linked to magmatism at the intermediate spreading Juan de Fuca Ridge. *Geology*, *34*, 209–212. https://doi.org/10.1130/g21969.1

Carbotte, S. M., Marjanović, M., Carton, H., Mutter, J. C., Canales, J. P., Nedimović, M. R., et al. (2013). Fine-scale segmentation of the crustal magma reservoir beneath the East Pacific Rise. *Nature Geoscience*, *6*, 866–870. https://doi.org/10.1038/ngeo1933

Caress, D. W., Burnett, M. S., & Orcutt, J. A. (1992). Tomographic image of the axial low-velocity zone at 12°50′N on the East Pacific Rise. *Journal of Geophysical Research*, *97*, 9243–9263. https://doi.org/10.1029/92jb00287

Carlson, R. L. (2011). The effect of hydrothermal alteration on the seismic structure of the upper oceanic crust: Evidence from Holes 504B and 1256D. *Geochemistry, Geophysics, Geosystems*, *12*, Q09013. https://doi.org/10.1029/2011GC003624

Carton, H., Carbotte, S. M., Mutter, J. C., Canales, J. P., Nedimovic, M. R., Newman, K., et al. (2008). Characteristics of the crustal magma body in the 2005–06 eruption area at 9°50′N on the East Pacific Rise from a 3D multi-channel seismic investigation. *Eos, Transactions, American Geophysical Union*, *89*(53). Fall Meet. Suppl., Abstract B23F-03

Chaussidon, M., & Marty, B. (1995). Primitive boron isotope composition of the mantle. *Science*, *269*, 383–386. https://doi.org/10.1126/science.269.5222.383

Coleman, R. G., & Peterman, Z. E. (1975). Oceanic plagiogranite. *Journal of Geophysical Research*, *80*, 1099–1108. https://doi.org/10.1029/jb080i008p01099

Collier, J. S., & Singh, S. C. (1997). Detailed structure of the top of the melt body beneath the East Pacific Rise at 9°40′N from waveform inversion of seismic reflection data. *Journal of Geophysical Research*, *102*(B9), 20287–20304. https://doi.org/10.1029/97JB01514

Coogan, L. A. (2003). Contaminating the lower crust in the Oman ophiolite. *Geology*, *31*(12), 1065–1068. https://doi.org/10.1130/G20129.1

Coogan, L. A., Mitchell, N. C., & O'Hara, M. J. (2003). Roof assimilation at fast spreading ridges: An investigation combining geophysical, geochemical, and field evidence. *Journal of Geophysical Research*, *108*(B1), ECV 2-1-ECV 2-14. https://doi.org/10.1029/2001JB001171

Coogan, L. A., Thompson, G., & MacLeod, C. J. (2002). A textural and geochemical investigation of high level gabbros from the Oman ophiolite: Implications for the role of the axial magma chamber at fast-spreading ridges. *Lithos*, *63*, 67–82. https://doi.org/10.1016/S0024-4937(02)00114-7

Crawford, W. C., Webb, S. C., & Hildebrand, J. A. (1999). Constraints on melt in the lower crust and Moho at the East Pacific Rise, 9°48′N, using seafloor compliance measurements. *Journal of Geophysical Research*, *104*, 2923–2939. https://doi.org/10.1029/1998jb900087

Currin, A., Wolff, P. E., Koepke, J., Almeev, R. R., Zhang, C., Zihlmann, B., et al. (2018). Chlorine-rich amphibole in deep layered gabbros as evidence for brine/rock interaction in the lower oceanic crust: A case study from the Wadi Wariyah, Samail Ophiolite, Sultanate of Oman. *Lithos*, *323*, 125–136. https://doi.org/10.1016/j.lithos.2018.09.015

DePaolo, D. J. (1981). Trace element and isotopic effects of combined wallrock assimilation and fractional crystallization. *Earth and Planetary Science Letters*, *53*, 189–202. https://doi.org/10.1016/0012-821X(81)90153-9

Detrick, R. S., Buhl, P., Vera, E., Mutter, J., Orcutt, J., Madsen, J., & Brocher, T. (1987). Multi-channel seismic imaging of a crustal magma chamber along the East Pacific Rise. *Nature*, *326*, 35–41. https://doi.org/10.1038/326035a0

Detrick, R. S., Toomey, D. R., & Collins, J. A. (1998). Three-dimensional upper crustal heterogeneity and anisotropy around Hole 504B from seismic tomography. *Journal of Geophysical Research*, *103*, 30485–30504. https://doi.org/10.1029/98JB02409

Dick, H. J. B., Macleod, C. J., Blum, P., Abe, N., Blackman, D. K., Bowles, J. A., et al. (2019). Dynamic accretion beneath a slow-spreading ridge segment: IODP Hole 1473A and the Atlantis Bank oceanic core complex. *Journal of Geophysical Research: Solid Earth*, *124*, 12631–12659. https://doi.org/10.1029/2018JB016858

Dunn, R. A., Toomey, D. R., & Solomon, S. C. (2000). Three-dimensional seismic structure and physical properties of the crust and shallow mantle beneath the East Pacific Rise at 9°30'N. *Journal of Geophysical Research*, *105*, 23537–23555. https://doi.org/10.1029/2000jb900210

Erdmann, M., Fischer, L. A., France, L., Zhang, C., Godard, M., & Koepke, J. (2015). Anatexis at the roof of an oceanic magma chamber at IODP Site 1256 (equatorial Pacific): An experimental study. *Contributions to Mineralogy and Petrology*, *169*(4), 39. https://doi.org/10.1007/s00410-015-1136-5

Erdmann, M., France, L., Fischer, L. A., Deloule, E., & Koepke, J. (2017). Trace elements in anatectic products at the roof of mid-ocean ridge magma chambers: An experimental study. *Chemical Geology*, *456*, 43–57. https://doi.org/10.1016/j.chemgeo.2017.03.004

Ernst, W. G., & Liu, J. (1998). Experimental phase-equilibrium study of Al- and Ti-contents of calcic amphibole in MORB— A semiquantitative thermobarometer. *American Mineralogist*, *83*(9–10), 952–969. https://doi.org/10.2138/am-1998-9-1004

Fischer, L. A., Erdmann, M., France, L., Wolff, P. E., Deloule, E., Zhang, C., et al. (2016). Trace element evidence for anatexis at oceanic magma chamber roofs and the role of partial melts for contamination of fresh MORB. *Lithos*, *260*, 1–8. https://doi.org/10.1016/j.lithos.2016.05.001

Fontaine, F. J., Olive, J.-A., Cannat, M., Escartin, J., & Perol, T. (2011). Hydrothermally-induced melt lens cooling and segmentation along the axis of fast- and intermediate-spreading centers. *Geophysical Research Letters*, *38*, L14307. https://doi.org/10.1029/2011GL047798

France, L., Ildefonse, B., & Koepke, J. (2009). Interactions between magma and hydrothermal system in Oman ophiolite and in IODP Hole 1256D: Fossilization of a dynamic melt lens at fast spreading ridges. *Geochemistry, Geophysics, Geosystems*, *10*, Q10O19. https://doi.org/10.1029/2009gc002652

France, L., Ildefonse, B., & Koepke, J. (2013). Hydrous magmatism triggered by assimilation of hydrothermally altered rocks in fossil oceanic crust (northern Oman ophiolite). *Geochemistry, Geophysics, Geosystems*, *14*, 2598–2614. https://doi.org/10.1002/ggge.20137

France, L., Ildefonse, B., Koepke, J., & Bech, F. (2010b). A new method to estimate the oxidation state of basaltic series from microprobe analyses. *Journal of Volcanology and Geothermal Research*, *189*, 340–346. https://doi.org/10.1016/j.jvolgeores.2009.11.023

France, L., Koepke, J., Ildefonse, B., Cichy, S. B., & Deschamps, F. (2010a). Hydrous partial melting in the sheeted dike complex at fast spreading ridges: Experimental and natural observations. *Contributions to Mineralogy and Petrology*, *160*(5), 683–704. https://doi.org/10.1007/s00410-010-0502-6

France, L., Koepke, J., MacLeod, C. J., Ildefonse, B., Godard, M., & Deloule, E. (2014). Contamination of MORB by anatexis of magma chamber roof rocks: Constraints from a geochemical study of experimental melts and associated residues. *Lithos*, *202–203*, 120–137. https://doi.org/10.1016/j.lithos.2014.05.018

Gannoun, A., Burton, K. W., Parkinson, I. J., Alard, O., Schiano, P., & Thomas, L. E. (2007). The scale and origin of the osmium isotope variations in mid-ocean ridge basalts. *Earth and Planetary Science Letters*, *259*, 541–556. https://doi.org/10.1016/j.epsl.2007.05.014

Gillis, K. M. (2002). The rootzone of an ancient hydrothermal system exposed in the Troodos ophiolite, Cyprus. *The Journal of Geology*, *110*(1), 57–74. https://doi.org/10.1086/324205

Gillis, K. M. (2008). The roof of an axial magma chamber: A hornfelsic heat exchanger. *Geology*, *36*(4), 299–302. https://doi.org/10.1130/g24590a.1

Gillis, K. M., & Coogan, L. A. (2002). Anatectic migmatites from the roof of an ocean ridge magma chamber. *Journal of Petrology*, *43*(11), 2075–2095. https://doi.org/10.1093/petrology/43.11.2075

Gillis, K. M., & Coogan, L. A. (2019). A review of the geological constraints on the conductive boundary layer at the base of the hydrothermal system at mid-ocean ridges. *Geochemistry, Geophysics, Geosystems*, *20*, 67–83. https://doi.org/10.1029/2018gc007878

Gillis, K. M., Coogan, L. A., & Chaussidon, M. (2003). Volatile behavior (Cl, F, B) in the roof of an axial magma chamber from the East Pacific Rise. *Earth and Planetary Science Letters*, *213*(3–4), 447–462. https://doi.org/10.1016/s0012-821x(03)00346-7

Gillis, K. M., & Roberts, M. (1999). Cracking at the magma-hydrothermal transition: Evidence from the Troodos ophiolite. *Earth and Planetary Science Letters*, *169*(3–4), 227–244. https://doi.org/10.1016/s0012-821x(99)00087-4

Gillis, K. M., Snow, J. E., Klaus, A., Abe, N., Adrião, Á. B., Akizawa, N., et al. (2014). Primitive layered gabbros from fast-spreading lower oceanic crust. *Nature*, *505*, 204–207. https://doi.org/10.1038/nature12778

Godard, M., Dautria, J. M., & Perrin, M. (2003). Geochemical variability of the Oman ophiolite lavas: Relationship with spatial distribution and paleomagnetic directions. *Geochemistry, Geophysics, Geosystems*, *4*, 8609. 10.1029/2002GC000452

Grimes, C. B., Ushikubo, T., Kozdon, R., & Valley, J. W. (2013). Perspectives on the origin of plagiogranite in ophiolites from oxygen isotopes in zircon. *Lithos*, *179*, 48–66. https://doi.org/10.1016/j.lithos.2013.07.026

Gualda, G. A. R., Ghiorso, M. S., Lemons, R. V., & Carley, T. L. (2012). Rhyolite-MELTS: A modified calibration of MELTS optimized for Silica-rich, fluid-bearing magmatic systems. *Journal of Petrology*, *53*(5), 875–890. https://doi.org/10.1093/petrology/egr080

Hayman, N. W., & Karson, J. A. (2009). Crustal faults exposed in the Pito Deep Rift: Conduits for hydrothermal fluids on the southeast Pacific Rise. *Geochemistry, Geophysics, Geosystems*, *10*, Q02013. https://doi.org/10.1029/2008GC002319

Hayman, N. W., Rioux, M., Anma, R., Tani, K., Dunkley, D. J., Crowley, J., & Schmitz, M. (2019). Accretion and oxidation of a super-fast-spread axial melt lens: TIMS and SIMS zircon analyses of the IODP Hole 1256D gabbros. *Lithos*, *348–349*, 105184. https://doi.org/10.1016/j.lithos.2019.105184

Holland, T., & Blundy, J. (1994). Non-ideal interactions in calcic amphiboles and their bearing on amphibole-plagioclase thermometry. *Contributions to Mineralogy and Petrology*, *116*(4), 433–447. https://doi.org/10.1007/bf00310910

Hooft, E. E. E., Detrick, R. S., & Kent, G. M. (1997). Seismic structure and indicators of magma budget along the southern East Pacific Rise. *Journal of Geophysical Research*, *102*(B12), 27319–27340. https://doi.org/10.1029/97JB02349

Humphris, S. E., & Cann, J. R. (2000). Constraints on the energy and chemical balances of the modern TAG and ancient Cyprus seafloor sulfide deposits. *Journal of Geophysical Research*, *105*(B12), 28477–28488. https://doi.org/10.1029/2000jb900289

Kelemen, P. B., Matter, J. M., Teagle, D. A. H., Coggon, J. A. & The Oman Drilling Project Science Team. (2020). Site GT3: Sheeted dike to gabbro transition. In *The Oman drilling Project science team, Proceedings of the Oman drilling Project*. College Station, TX: International Ocean Discovery Program. https://doi.org/10.14379/OmanDP.proc

Kent, G. M., Harding, A. J., & Orcutt, J. A. (1990). Evidence for a smaller magma chamber beneath the East Pacific Rise at 9°30′ N. *Nature*, *344*(6267), 650–653. https://doi.org/10.1038/344650a0

Kent, G. M., Harding, A. J., & Orcutt, J. A. (1993). Distribution of magma beneath the East Pacific Rise between the clipperton transform and the 9°17′N deval from forward modeling of common depth point data. *Journal of Geophysical Research*, *98*(B8), 13945–13969. https://doi.org/10.1029/93jb00705

Koepke, J., Berndt, J., & Bussy, F. (2003). An experimental study on the shallow-level migmatization of ferrogabbros from the Fuerteventura Basal Complex, Canary Islands. *Lithos*, *69*, 105–125. https://doi.org/10.1016/s0024-4937(03)00049-5

Koepke, J., Berndt, J., Feig, S. T., & Holtz, F. (2007). The formation of SiO_2-rich melts within the deep oceanic crust by hydrous partial melting of gabbros. *Contributions to Mineralogy and Petrology*, *153*, 67–84. https://doi.org/10.1007/s00410-006-0135-y

Koepke, J., Christie, D. M., Dziony, W., Holtz, F., Lattard, D., Maclennan, J., et al. (2008). Petrography of the dike-gabbro transition at IODP Site 1256 (equatorial Pacific): The evolution of the granoblastic dikes. *Geochemistry, Geophysics, Geosystems*, *9*, Q07O09. https://doi.org/10.1029/2008GC001939

Koepke, J., Feig, S. T., Snow, J., & Freise, M. (2004). Petrogenesis of oceanic plagiogranites by partial melting of gabbros: An experimental study. *Contributions to Mineralogy and Petrology*, *146*, 414–432. https://doi.org/10.1007/s00410-003-0511-9

Koepke, J., France, L., Müller, T., Faure, F., Goetze, N., Dziony, W., & Ildefonse, B. (2011). Gabbros from IODP Site 1256, equatorial Pacific: Insight into axial magma chamber processes at fast spreading ocean ridges. *Geochemistry, Geophysics, Geosystems*, *12*, Q09014. https://doi.org/10.1029/2011gc003655

Koepke, J., Schoenborn, S., Oelze, M., Wittmann, H., Feig, S. T., Hellebrand, E., et al. (2009). Petrogenesis of crustal wehrlites in the Oman ophiolite: Experiments and natural rocks. *Geochemistry, Geophysics, Geosystems*, *10*, Q10002. https://doi.org/10.1029/2009GC002488

Koepke, J., & Zhang, C. (2020). Axial melt lens dynamics at fast-spreading mid-ocean ridges. In F. Vetere (Ed.), *Dynamic magma evolution* (p. 224). AGU Geophysical Monograph Series (ISBN: 978-1-119-52113-6.

Lagabrielle, Y., & Cormier, M.-H. (1999). Formation of large summit troughs along the East Pacific Rise as collapse calderas: An evolutionary model. *Journal of Geophysical Research*, *104*(B6), 12971–12988. https://doi.org/10.1029/1999JB900015

Lamoureux, G., Ildefonse, B., & Mainprice, D. (1999). Modelling the seismic properties of fast-spreading ridge crustal low-velocity zones: Insights from Oman gabbro textures. *Tectonophysics*, *312*(2–4), 283–301. https://doi.org/10.1016/S0040-1951(99)00183-3

Lejeune, A.-M., & Richet, P. (1995). Rheology of crystal-bearing silicate melts: An experimental study at high viscosities. *Journal of Geophysical Research*, *100*, 4215–4229. https://doi.org/10.1029/94JB02985

Leroux, P., Shirey, S., Hauri, E., Perfit, M., & Bender, J. (2006). The effects of variable sources, processes and contaminants on the composition of northern EPR MORB (8-10°N and 12-14°N): Evidence from volatiles (H_2O, CO_2, S) and halogens (F, Cl). *Earth and Planetary Science Letters*, *251*, 209–231. https://doi.org/10.1016/j.epsl.2006.09.012

Lesher, C. E., & Spera, F. J. (2015). Thermodynamic and transport properties of silicate melts and magma. In H. Sigurdsson, B. Houghton, H. Rymer, J. Stix, & S. McNutt (Eds.), *The encyclopedia of volcanoes* (pp. 113–141). ScienceDirect.

Lilley, M. D., Butterfield, D. A., Lupton, J. E., & Olson, E. J. (2003). Magmatic events can produce rapid changes in hydrothermal vent chemistry. *Nature*, *422*(6934), 878–881. https://doi.org/10.1038/nature01569

Lissenberg, C. J., MacLeod, C. J., & Bennett, E. N. (2019). Consequences of a crystal mush-dominated magma plumbing system: A mid-ocean ridge perspective. *Philosophical Transactions of the Royal Society A*, *377*, 20180014. https://doi.org/10.1098/rsta.2018.0014

Lowell, R. P., Farough, A., Hoover, J., & Cummings, K. (2013). Characteristics of magma-driven hydrothermal systems at oceanic spreading centers. *Geochemistry, Geophysics, Geosystems*, *14*, 1756–1770. https://doi.org/10.1002/ggge.20109

Macdonald, K. C., Scheirer, D. S., & Carbotte, S. M. (1991). Mid-ocean ridges: Discontinuities, segments and giant cracks. *Science*, *253*, 986–994. https://doi.org/10.1126/science.253.5023.986

MacLeod, C. J., Johan Lissenberg, C., & Bibby, L. E. (2013). "Moist MORB" axial magmatism in the Oman ophiolite: The evidence against a mid-ocean ridge origin. *Geology*, *41*(4), 459–462. https://doi.org/10.1130/g33904.1

MacLeod, C. J., & Rothery, D. A. (1992). Ridge axial segmentation in the Oman ophiolite: Evidence from along-strike variations in the sheeted dyke complex. In L. M. Parson, B. J. Murton, & P. Browning (Eds.), *Ophiolites and their modern analogues* (pp. 39–63). London. Geological Society - Special Publications. https://doi.org/10.1144/GSL.SP.1992.060.01.03

MacLeod, C. J., & Yaouancq, G. (2000). A fossil melt lens in the Oman ophiolite: Implications for magma chamber processes at fast spreading ridges. *Earth and Planetary Science Letters*, *176*, 357–373. https://doi.org/10.1016/S0012-821X(00)00020-0

Marjanović, M., Carbotte, S. M., Carton, H., Nedimović, M. R., Canales, J. P., & Mutter, J. C. (2018). Crustal magmatic system beneath the East Pacific Rise (8º20′ to 10º10′ N): Implications for tectono-magmatic segmentation and melt transport at fast-spreading ridges. *Geochemistry, Geophysics, Geosystems*, *19*, 4584–4611 10.1029/2018GC007590

Marjanović, M., Fuji, N., Singh, S. C., Belahi, T., & Escartín, J. (2017). Seismic signatures of hydrothermal pathways along the East Pacific Rise between 9°16' and 9°56'N. *Journal of Geophysical Research: Solid Earth*, *122*, 10241–10262. https://doi.org/10.1002/2017JB015004

Marjanovic, M., Carbotte, S. M., Carton, H., Nedimovic, M. R., Mutter, J. C., & Canales, J. P. (2014). A multi-sill magma plumbing system beneath the axis of the East Pacific Rise. *Nature Geoscience*, *7*, 825–829. https://doi.org/10.1038/ngeo2272

Marjanovic, M., Carton, H., Carbotte, S. M., Nedimovic, M. R., Mutter, J. C., & Canales, J. P. (2015). Distribution of melt along the East Pacific Rise from 9°30′ to 10°N from an amplitude variation with angle of incidence (AVA) technique. *Geophysical Journal International*, *203*, 1–21. https://doi.org/10.1093/gji/ggv251

Michael, P. J., & Cornell, W. C. (1998). Influence of spreading rate and magma supply on crystallisation and assimilation beneath mid ocean ridges: Evidence from chlorine and major element chemistry of mid-ocean ridge basalts. *Journal of Geophysical Research*, *103*(B8). 18325–1356. https://doi.org/10.1029/98jb00791

Müller, R. D., Sdrolias, M., Gaina, C., & Roest, W. R. (2008). Age, spreading rates, and spreading asymmetry of the world's ocean crust. *Geochemistry, Geophysics, Geosystems*, *9*(4), Q04006. https://doi.org/10.1029/2007GC001743

Müller, T., Koepke, J., Garbe-Schönberg, C.-D., Dietrich, M., Bauer, U., & Wolff, P. E. (2017). Anatomy of a frozen axial melt lens from a fast-spreading paleo-ridge (Wadi Gideah, Oman ophiolite). *Lithos*, *272–273*, 31–45. https://doi.org/10.1016/j.lithos.2016.11.022

Natland, J. H., & Dick, H. J. B. (1996). Melt migration through high-level gabbroic cumulates of the East Pacific Rise at Hess Deep: The origin of magma lenses and the deep crustal structure of fast-spreading ridges. In C. Mével, K. Gillis, J. F. Allan, & P. S. Meyer (Eds.), *Proceedings of the ocean drilling program, scientific results* (pp. 21–58). College Station, TX. Ocean Drilling Program.

Nedimovicc, M. R., Carbotte, S. M., Harding, A. J., Detrick, R. S., Canales, J. P., Diebold, J. B., et al. (2005). Frozen magma lenses below the oceanic crust. *Nature*, *436*(7054), 1149–1152.

Nehlig, P. (1993). Interactions between magma chambers and hydrothermal systems: Oceanic and ophiolitic constraints. *Journal of Geophysical Research*, *98*(11), 19621–19633. https://doi.org/10.1029/93jb01822

Nehlig, P., Juteau, T., Bendel, V., & Cotten, J. (1994). The root zones of oceanic hydrothermal systems: Constraints from the samail ophiolite (Oman). *Journal of Geophysical Research*, *99*(B3), 4703–4713. https://doi.org/10.1029/93jb02663

Nicolas, A., & Boudier, F. (1991). Rooting of the sheeted dike complex in the Oman ophiolite. In T. Peters, A. Nicolas, & R. G. Coleman (Eds.), *Ophiolite genesis and evolution of the oceanic lithosphere* (pp. 39–54). Sultanate of Oman: Ministry of Petroleum and Minerals. https://doi.org/10.1007/978-94-011-3358-6_4

Nicolas, A., Boudier, F., & France, L. (2009). Subsidence in magma chamber and the development of magmatic foliation in Oman ophiolite gabbros. *Earth and Planetary Science Letters*, *284*, 76–87. https://doi.org/10.1016/j.epsl.2009.04.012

Nicolas, A., Boudier, F., Ildefonse, B., & Ball, E. (2000). Accretion of Oman and United Arab Emirates ophiolite: Discussion of a new structural map. *Marine Geophysical Researches*, *21*, 147–179. https://doi.org/10.1023/A:1026769727917

Nicolas, A., Boudier, F., Koepke, J., France, L., Ildefonse, B., & Mevel, C. (2008). Root zone of the sheeted dike complex in the Oman ophiolite. *Geochemistry, Geophysics, Geosystems*, *9*, Q05001. https://doi.org/10.1029/2007gc001918

Nicolas, A., Mainprice, D., & Boudier, F. (2003). High-temperature seawater circulation throughout crust of oceanic ridges: A model derived from the Oman ophiolites. *Journal of Geophysical Research*, *108*(B8), 2371. https://doi.org/10.1029/2002jb002094

Participants, Conference (1972). Penrose field conference on ophiolites. *Geotimes*, *17*, 24–25.

Peacock, S. M. (1989). Thermal modeling of metamorphic pressure-temperature-time paths: A forward approach. In F. S. Spear, & S. M. Peacock (Eds.), *Metamorphic pressure-temperature-time paths, short course in geology* (pp. 57–102). Washington, DC: American Geophysical Union.

Pouchou, J. L., & Pichoir, F. (1991). Quantitative analysis of homogeneous or stratified microvolumes applying the model "PAP". In K. F. J. Heinrich, & D. E. Newbury (Eds.), *Electron probe quantification* (pp. 31–75). New York. Plenum Press.

Rioux, M., Bowring, S., Kelemen, P., Gordon, S., Dudás, F., & Miller, R. (2012). Rapid crustal accretion and magma assimilation in the Oman-U.A.E. ophiolite: High precision U-Pb zircon geochronology of the gabbroic crust. *Journal of Geophysical Research*, *117*, B07201. https://doi.org/10.1029/2012JB009273

Rothery, D. A. (1983). The base of a sheeted dyke complex, Oman ophiolite: Implications for magma chambers at oceanic spreading axes. *Journal of the Geological Society*, *140*(2), 287–296. https://doi.org/10.1144/gsjgs.140.2.0287

Rubin, K. H., & Sinton, J. M. (2007). Inferences on mid-ocean ridge thermal and magmatic structure from MORB compositions. *Earth and Planetary Science Letters*, *260*, 257–276. https://doi.org/10.1016/j.epsl.2007.05.035

Sauerzapf, U., Lattard, D., Burchard, M., & Engelmann, R. (2008). The titanomagnetite-ilmenite equilibrium: New experimental data and thermo-oxybarometric application to the crystallization of basic to intermediate rocks†. *Journal of Petrology*, *49*, 1161–1185. https://doi.org/10.1093/petrology/egn021

Singh, S. C., Collier, J. S., Harding, A. J., Kent, G. M., & Orcutt, J. A. (1999). Seismic evidence for a hydrothermal layer above the solid roof of the axial magma chamber at the southern East Pacific Rise. *Geology*, *27*(3), 219–222. https://doi.org/10.1130/0091-7613(1999)027<0219:sefahl>2.3.co;2

Singh, S. C., Kent, G. M., Collier, J. S., Harding, A. J., & Orcutt, J. A. (1998). Melt to mush variations in crustal magma properties along the ridge crest at the southern East Pacific Rise. *Nature*, *394*(6696), 874–878. https://doi.org/10.1038/29740

Sinton, J. M., & Detrick, R. S. (1992). Mid-ocean ridge magma chambers. *Journal of Geophysical Research*, *97*, 197–216. https://doi.org/10.1029/91JB02508

Spear, F. S. (1989). Petrologic determination of metamorphic pressure-temperature-time paths. In *Metamorphic pressure-temperature-time paths*, In F. S. Spear, & S. M. Peacock (Eds.), Short Course in Geology, *7* (pp. 1–55). Washington, D. C. AGU.

Spear, F. S., & Peacock, S. M. (1990). *Metamorphic P-T-t paths: Program manual and computer exercises for the calculation of metamorphic phase equilibria, pressure-temperature-time paths and thermal evolution of orogenic belts* (p. 188). Dallas, Texas. Geological Society of America short course.

Spear, F. S., Peacock, S. M., Kohn, M. J., Florence, F. P., & Menard, T. (1991). Computer programs for petrologic PTt path calculations. *American Mineralogist*, *76*(11–12), 2009–2012.

Teagle, D. A. H., Ildefonse, B., Blum, P., & The Expedition 335 Scientists. (2012). *Proceedings of the international Ocean Drilling Program*, *335*. Tokyo. Integrated Ocean Drilling Program Management International, Inc. http://dx.doi.org/10.2204/iodp.proc.335.2012

Tolstoy, M., Waldhauser, F., Bohnenstiehl, D. R., Weekly, R. T., & Kim, W.-Y. (2008). Seismic identification of along-axis hydrothermal flow on the East Pacific rise. *Nature*, *451*(7175), 181–184. https://doi.org/10.1038/nature06424

Wanless, V. D., Perfit, M. R., Ridley, W. I., & Klein, E. (2010). Dacite petrogenesis on mid-ocean ridges: Evidence for oceanic crustal melting and assimilation. *Journal of Petrology*, *51*(12), 2377–2410. https://doi.org/10.1093/petrology/egq056

Wanless, V. D., Perfit, M. R., Ridley, W. I., Wallace, P. J., Grimes, C. B., & Klein, E. M. (2011). Volatile abundances and oxygen isotopes in basaltic to dacitic lavas on mid-ocean ridges: The role of assimilation at spreading centers. *Chemical Geology*, *287*(1–2), 54–65. https://doi.org/10.1016/j.chemgeo.2011.05.017

Warren, C. J., Parrish, R. R., Waters, D. J., & Searle, M. P. (2005). Dating the geologic history of Oman's Semail ophiolite: Insights from U-Pb geochronology. *Contributions to Mineralogy and Petrology*, *150*, 403–422. https://doi.org/10.1007/s00410-005-0028-5

Warren, C. J., Searle, M. P., Parrish, R. R., & Waters, D. J. (2007). Reply to Comment by F. Boudier and A. Nicolas on "Dating the geologic history of Oman's Semail Ophiolite: Insights from U-Pb geochronology" by C.J. Warren, R.R. Parrish, M.P. Searle and D.J. Waters. *Contributions to Mineralogy and Petrology*, *154*, 115–118. https://doi.org/10.1007/s00410-007-0182-z

Wilson, D. S., Teagle, D. A. H., Alt, J. C., Banerjee, N. R., Umino, S., Miyashita, S., et al. (2006). Drilling to gabbro in intact ocean crust. *Science*, *312*, 1016–1020. https://doi.org/10.1126/science.1126090

Xu, G., Jackson, D. R., Bemis, K. G., & Rona, P. A. (2014b). Time-series measurement of hydrothermal heat flux at the Grotto mound, Endeavour Segment, Juan de Fuca Ridge. *Earth and Planetary Science Letters*, *404*, 220–231. https://doi.org/10.1016/j.epsl.2014.07.040

Xu, M., Pablo Canales, J., Carbotte, S. M., Carton, H., Nedimović, M. R., & Mutter, J. C. (2014a). Variations in axial magma lens properties along the East Pacific Rise (9°30′N-10°00′N) from swath 3-D seismic imaging and 1-D waveform inversion. *Journal of Geophysical Research: Solid Earth*, *119*, 2721. https://doi.org/10.1002/2013JB010730

Zhang, C., Koepke, J., France, L., & Godard, M. (2017b). Felsic plutonic rocks from IODP Hole 1256D, Eastern Pacific: Implications for the nature of the axial melt lens at fast-spreading mid-ocean ridges. *Journal of Petrology*, *58*, 1535–1565. https://doi.org/10.1093/petrology/egx064

Zhang, C., Koepke, J., Kirchner, C., Götze, N., & Behrens, H. (2014). Rapid hydrothermal cooling above the axial melt lens at fast-spreading mid-ocean ridge. *Scientific Reports*, *4*, 6342. https://doi.org/10.1038/srep06342

Zhang, C., Wang, L.-X., Marks, M. A. W., France, L., & Koepke, J. (2017a). Volatiles (CO_2, S, F, Cl, Br) in the dike-gabbro transition zone at IODP Hole 1256D: Magmatic imprint versus hydrothermal influence at fast-spreading mid-ocean ridge. *Chemical Geology*, *459*, 43–60. https://doi.org/10.1016/j.chemgeo.2017.04.002

Zihlmann, B., Müller, S., Coggon, R. M., Koepke, J., Garbe-Schönberg, D., & Teagle, D. A. H. (2018). Hydrothermal fault zones in the lower oceanic crust: An example from Wadi Gideah, Samail ophiolite, Oman. *Lithos*, *323*, 103–124. https://doi.org/10.1016/j.lithos.2018.09.008